LA-9551-MS

C.3

Chemistry and Spectroscopy of a Fireball

Los Alamos
Los Alamos National Laboratory
Los Alamos, New Mexico 87545

Edited by Glenda Ponder, ESS Division

Chemistry and Spectroscopy
of a Fireball

J. Zinn
C. D. Sutherland
C. K. Mitchell*

*EG&G. 1100 4th Street, Los Alamos. NM 87544.

Los Alamos
Los Alamos National Laboratory
Los Alamos, New Mexico 87545

CONTENTS

Fig. 13. Ivy-King fireball brightness at 10.7 to 12.9 ms; (a) data and (b) calculated. The calculated curve is of a blackbody at 10000 K as seen through 3.0×10^{19} molec/cm^2 of HNO$_2$ plus 6.0×10^{18} molec/cm^2 of NO$_2$ plus 1.5×10^{20} molec/cm^2 of O$_3$.

Fig. 14. Ivy-King fireball brightness at 20.9 ms; (a) data and (b) calculated. The calculated curve is of a blackbody at 7000 K as seen through 3.0×10^{19} molec/cm^2 of HNO$_2$ plus 5.6×10^{18} molec/cm^2 of NO$_2$ plus 1.2×10^{20} molec/cm^2 of O$_3$ plus 3.0×10^{18} hot molec/cm^2 of NO$_2$.

Fig. 15. Ivy-King fireball brightness at 42.4 ms; (a) data and (b) calculated. The calculated curves include a blackbody at 4000 K (1) bare and (2) as seen through 3.0×10^{19} molec/cm^2 of HNO$_2$ plus 4.5×10^{18} molec/cm^2 of NO$_2$ plus 1.0×10^{20} molec/cm^2 of O$_3$ plus 3.0×10^{20} molec/cm^2 of hot NO$_2$.

Fig. 16. Column densities of O$_3$, HNO$_2$, and NO$_2$ as inferred from the Ivy-King spectrum. Also shown are the shock temperatures derived from the radius-time data.

Fig. 17. Potential energy curves for O$_2^-$, O$_2$ and O$_2^+$ (from Krupenie[7]).

Fig. 18. Time-retarded path integrals of gamma ray and neutron energy deposition along Navajo chord (1) 3-D Monte Carlo computations (2) spherical fit by Eqs. (1) through (11).

Fig. 19. Time-retarded chord integrals of the computed concentrations of O$_3$, HNO$_2$, and O$_3$. (Navajo)

Fig. 20. Production efficiencies or O$_3$, HNO$_2$ and NO$_2$ vs detector time. Solid lines and points are experimental data (see Fig. 4). The dashed curves are computed with the model. (Navajo)

Fig. 21. Computed chord column densities of O$_2^*$(V3) and O$_2$($^1\Sigma$) vs detector time. (Navajo)

Fig. 22. Column densities of O$_3$, HNO$_2$ and NO$_2$ from the King event. Solid curves and points are experimental (see Fig. 16). Dashed curves are computed with the model.

Fig. 23. Computed radiant power vs time curve for a generic 1-Mt explosion as convolved with the spectral response function of a bare silicon detector. Dashed curve represents neutron-induced flourescence signal.

CHEMISTRY AND SPECTROSCOPY OF A FIREBALL

by

J. Zinn, C. D. Sutherland, and C. K. Mitchell

ABSTRACT

This report describes the analysis of streak spectra from the 1956 Redwing-Navajo chord experiment and the 1952 Ivy-King experiment. Column densities of O_3, HNO_2, NO_2, and vibrationally excited O_2 are inferred from the spectra and related to computed column densities of gamma ray and neutron energy deposition. We also describe a fireball radiation transport, hydrodynamics, and chemistry computer model, which we use to make theoretical predictions of the column densities of molecular absorbers outside of a fireball. Computed results for Navajo and King are compared with the experimental data. We also show a computation of radiant power vs time for a generic 1-Mt fireball.

I. INTRODUCTION

This report constitutes an update of our 1980 classified report. It is designed to be unclassified; therefore it omits precise weapon yields, outputs, and classified references.

The theoretical analysis in this report is based on a new, more advanced computer model that includes radiation, hydrodynamics, and photochemistry in a coupled self-consistent manner. We describe again the data analysis of the 1956 Navajo chord spectroscopy experiment and the 1952 King experiment, and compare the new theoretical model results with those data.

Practical interest in these matters relates to the effects of the non-equilibrium chemistry on the optical and infrared emission from a nuclear fireball, particularly in the early time regime up through first maximum. It is well known that the early fireball light from moderate-to-high-yield explosions is attenuated by chemicals that we identify collectively as "smog" (NO_2, O_3, HNO_2, etc.), largely the products of ionization by gamma rays and neutrons. We are now able to make reasonable quantitative computations of the amount of smog that is produced, and its effect on a fireball optical signature. We will show a few examples of computed bhangmeter power vs time curves with and without the smog.

The chemistry model in the present code is new. The lumped ion chemistry reaction set is revised substantially. We also attempt to include the non-LTE processes associated with the vibrationally excited O_2 states, whose Schumann-Runge absorption bands have puzzled fireball spectroscopists since the 1950s. The model appears to account for the spectroscopic observations, after adjustment of a few free parameters.

The neutron deposition algorithm is also revised, so that it now takes account of the deposition of the neutron kinetic energy and the deposition of energy from (n,p) and (n,γ) capture reactions as distinct and separate processes.

II. NAVAJO CHORD EXPERIMENT

There are not many sources of good quantitative data on smog composition. Unquestionably the best data that were obtained were from the "chord" experiment of event Redwing-Navajo. Because it was a key experiment, and because we have improved our understanding of it a bit since 1980, we will describe it again in some detail.

The experimental setup is shown in Fig. 1. Light from a very large (5 ft x 8 ft) explosive-driven argon flashlamp was received by a time-resolving spectrograph, along a line of sight that passed 500 m from the location of the nuclear device. (The yield range of Navajo was one to several megatons.) The argon flash was timed to begin 10 μs before the nuclear detonation and lasted for 50 μs. The spectrograph recorded the spectrum of the flash before the detonation and continuously for 40 μs thereafter, while the intervening air was being dosed, first by prompt gamma rays and later by neutrons.

We assume that the spectral intensity of the argon flash was constant in time. To the extent that that assumption is true, the ratio of the measured intensity at a given wavelength at some instant after the nuclear detonation to the intensity at the same wavelength before the detonation is the attenuation due to chemicals produced in the air along the chord by the effects of the detonation (i.e., by the gamma rays and neutrons). If we measure the
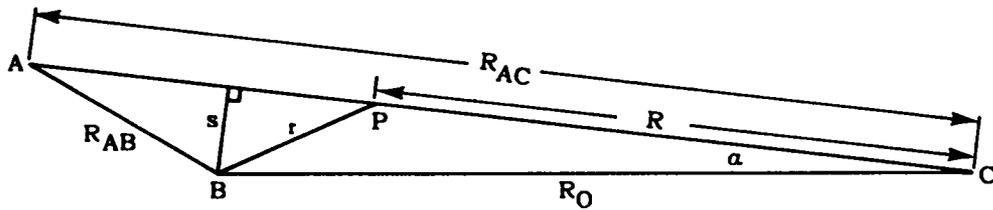
A   Argon light source barge
B   Shot barge
C   Spectrograph station

R_{AC} = 5704 m
R_O = 4969 m
R_{AB} = 908 m
s = 498 m
R = 4944 m At point of
closest approach

Fig. 1. Navajo chord geometry.

attenuation at $\underline{n}$ suitably chosen wavelengths, then in principle we can determine the column densities of $\underline{n}$ absorbing species along the chord, if we know their absorption cross sections. Actually we can measure the attenuation at many more wavelengths than we need; therefore the solutions for the column densities are overdetermined.

The gamma and neutron dosage along the chord was insufficient to cause significant heating of the air, so that we can assume ambient-temperature absorption cross sections. Moreover, the visible and ultraviolet flux from the explosion was insufficient to complicate the chemistry with photochemical reactions. Therefore, Navajo was an ideal baseline experiment for characterizing the chemistry of irradiated cold air.

The absorbing species that were identified are NO_2, HNO_2, O_3, and several high vibrational states of O_2. The vibrationally excited O_2 implies an extreme departure from Boltzmann equilibrium, and we will expand on this point later on.

We also have quantitative information about the energy deposited along the chord by the neutrons and gamma rays. This comes from detailed nuclear device output computations, followed by 3-D Monte Carlo computations that treat the transport of neutrons and gamma rays out of the device and test assembly and through the intervening air. Figure 2 shows the computed line-of-sight integrals of the gamma and neutron energy deposited along the chord as a function of "detector time." Detector time means time measured at the spectrograph relative to the time of first arrival of gamma rays or other photons from the bomb. The energy deposition integrals are in "retarded time;" i.e., they are computed with proper allowance for the finite velocity of light.

From the spectra we deduced column densities of NO_2, HNO_2, and O_3 along the chord as functions of detector time. These are plotted in Fig. 3. By the nature of the optical setup, the column density integrals are automatically in retarded-time geometry (i.e., in the same frame of reference as the energy deposition integrals in Fig. 2).
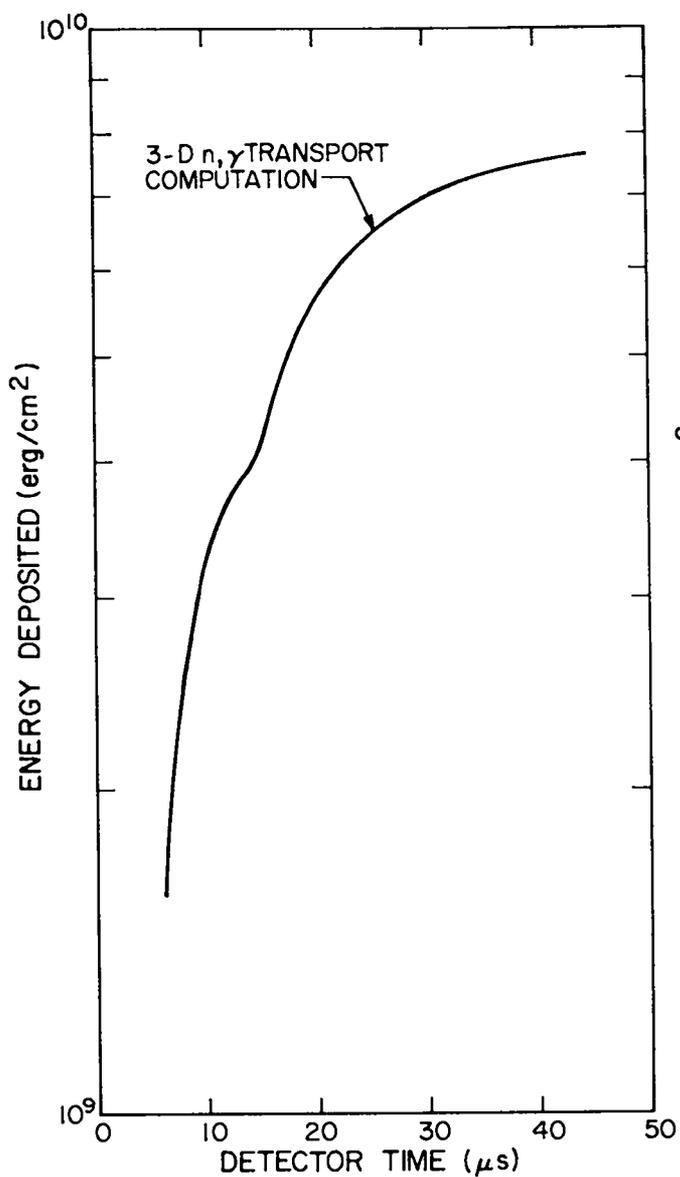
Fig. 2. Time–retarded path integral of computed gamma ray and neutron energy deposition along Navajo chord.
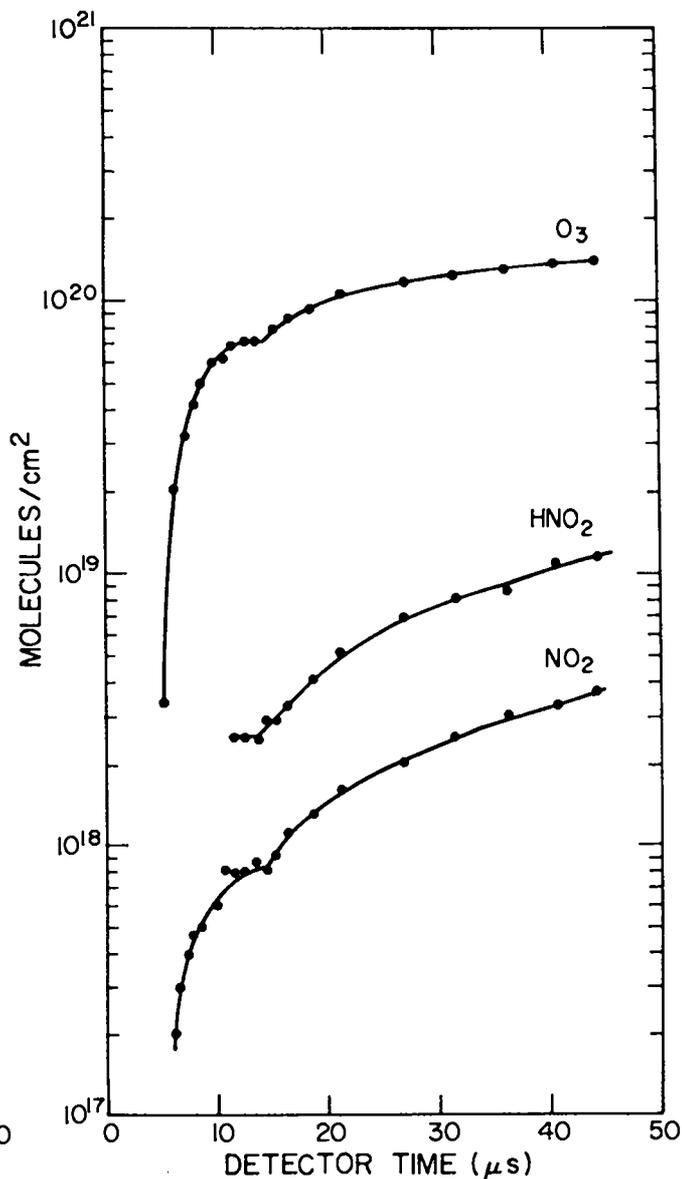
Fig. 3. Measured column densities of O_3, HNO_2, and NO_2 vs detector time. (Navajo)

5

An interesting quantity, derivable from the data in Fig. 3 and the radiation dose computations in Fig. 2, is the quotient, which we call the "production efficiency" of each given chemical species. The production efficiency is the number of molecules formed and existing at a given time per erg of radiation deposited. The production efficiencies for NO_2, HNO_2, and O_3 derived from the quantities in Figs. 2 and 3 are plotted in Fig. 4. If we assume that each 35 eV of ionizing radiation deposited produces one ion-electron pair, on the average, then we can interpret the production efficiency data in Fig. 4 in terms of molecules of each species existing at time t per ion pair produced by the neutrons and gammas.

For the case of O_3 the production efficiency is very nearly a constant, independent of time, and corresponds to about 1.0 ozone molecule per ion pair. For NO_2 and HNO_2 the production efficiencies are by no means constant. In fact they are almost exponentially increasing functions of time. At times in the past it has been assumed, for lack of this detailed data analysis, that the production efficiencies of NO_2 and HNO_2 were just constants, or perhaps different constants for production by neutrons or by gamma rays. Figure 4 shows that that was a rather poor approximation. (However, the error bars are probably ±30%, so other opinions can be sustained.)

It is quite reasonable that the production efficiency of O_3 should be constant while the production efficiencies of NO_2 and HNO_2 should increase with time. In the initial (electron cascade) process of ionization of air by neutrons and gammas many molecules are also dissociated into atoms. Computations by Myers and Schoonover[1] for 60-km altitude indicate that about 0.35 $O(^3P)$ and $O(^1D)$ atoms, 0.36 $N(^4S)$ atoms and 0.42 $N(^2D)$ atoms should be formed per ion pair. Subsequently, on a sub-microsecond time scale, the $O(^3P)$ and $O(^1D)$ atoms should become attached to O_2 to form O_3, and the $N(^2D)$ atoms should react with O_2 to form NO and more O_3. Also on a sub-microsecond time scale, where the ion densities are high the primary positive ions N_2^+, O_2^+, N^+ and O^+ recombine with electrons to form more N and O atoms, more NO and more O_3. Most of the ozone that forms comes from these very fast reactions; hence it is formed very quickly.
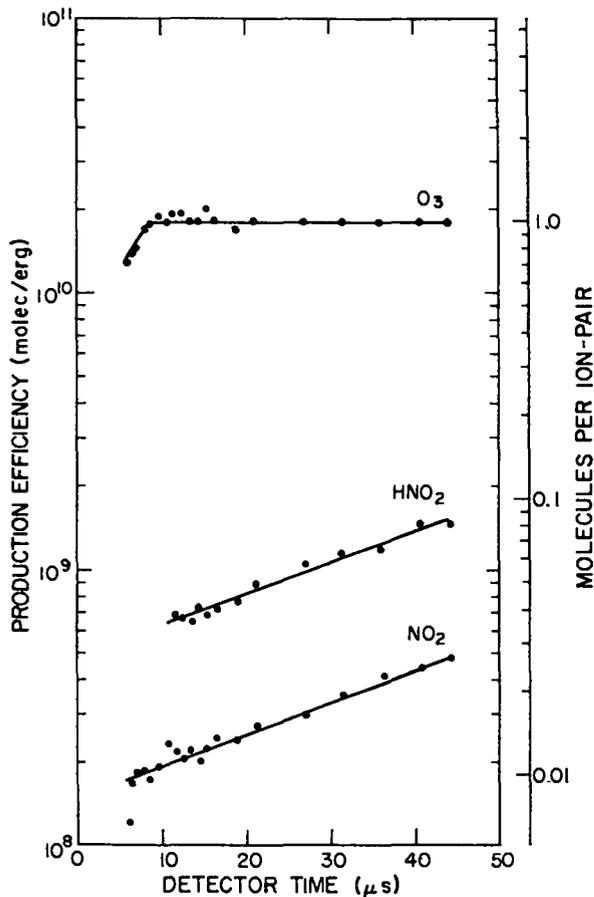
Fig. 4. Production efficiencies of O_3, HNO_2, and NO_2, as derived from the measured species concentrations in Fig. 3 and the computed energy deposition integrals in Fig. 2. (Navajo)

On a slightly slower time scale, and where the ion-electron densities are not very large (i.e., $<10^{14}$ cm^{-3}), the primary ions react first with N_2 and O_2 and subsequently with H_2O to form hydrated ions, OH radicals, and some HNO_2. The hydrated ions then react with electrons and negative ions to form H atoms, which combine rapidly with O_2 to form HO_2. On a longer time scale the HO_2, OH, and O_3 react with the N and NO to form NO_2 and more HNO_2. The NO_2 and HNO_2- forming reactions are basically <u>second</u> <u>order</u> (i.e., quadratic) in the concentration of ion-pairs initially formed. Therefore the production efficiencies of NO_2 and HNO_2 should increase with time. They should also be proportional to the energy deposition density—a fact that is not obvious from Fig. 4. They also depend on the relative humidity.

7

Figures 3 and 4 are really summary graphs. Some of the more basic data are shown in Figs. 5 through 8. Figure 5(a) shows the radiometrically reduced spectrum of the argon flashlamp just before the arrival of gamma rays in the line of sight. The spectrum resembles that of a 17000 K blackbody attenuated by about 6×10^{17} molec/cm^2 of ozone, the amount that one would expect to exist in the 5-km optical path in normal sea level air [Fig. 5(b)]. The absorption feature at 3100 Å, in the light of very recent experiments by W. C. Davis (Los Alamos National Laboratory, personal communication) appears to be an artifact associated with the response of the spectrographic film, and has no deeper significance.

Figures 6(a) and (b) show the changes in the spectrum at 2- and 4-μs detector time, produced by irradiation of the air along the chord by gamma rays from the detonation. An absorption feature develops at 3100 Å and another at 3370 Å, both increasing in intensity as more gamma rays reach the chord. Additional continuum absorption develops over the spectral range 2900 to 3200 Å. The two band absorptions are attributed to the (0,12) and (0,14) Schumann–Runge transitions of molecular O_2. The continuum is mainly due to O_3.

From the data in Figs. 6(a) and (b) one can calculate spectral attenuation factors, I/I_0 and corresponding optical depths $\tau = \ln(I_0/I)$ Figures 7(a) and (b) are spectra at somewhat later times, 7.9 and 15.1 μs, presented in the form of τ vs λ. The spectra show the (0,12), (0,13), (0,14), and (0,15) Schumann–Runge bands of O_2^*, superimposed on a growing continuum, which is due to O_3. Absorption bands due to NO_2 and HNO_2 have also appeared, and they increase with time. At 7.9 μs the radiation dosage is entirely due to gamma rays. At 15.1 μs the neutrons are beginning to contribute.

Figure 8 illustrates another way of analyzing the data, using a spectrum at 7 μs. The figure shows the reference argon flash spectrum, the 7-μs data spectrum, and a computer-generated "synthetic" spectrum. The synthetic spectrum is formed from the reference spectrum multiplied by a set of attenuation factors produced by an assumed absorbing layer composed of 2.15×10^{18} molec/cm^2 of HNO_2, 2.7×10^{18} molec/cm^2 of NO_2, and 1.7×10^{19} molec/cm^2 of O_3. Those column densities are the ones that appear to produce the best fit to the data spectrum, but comparison with the data shows that some
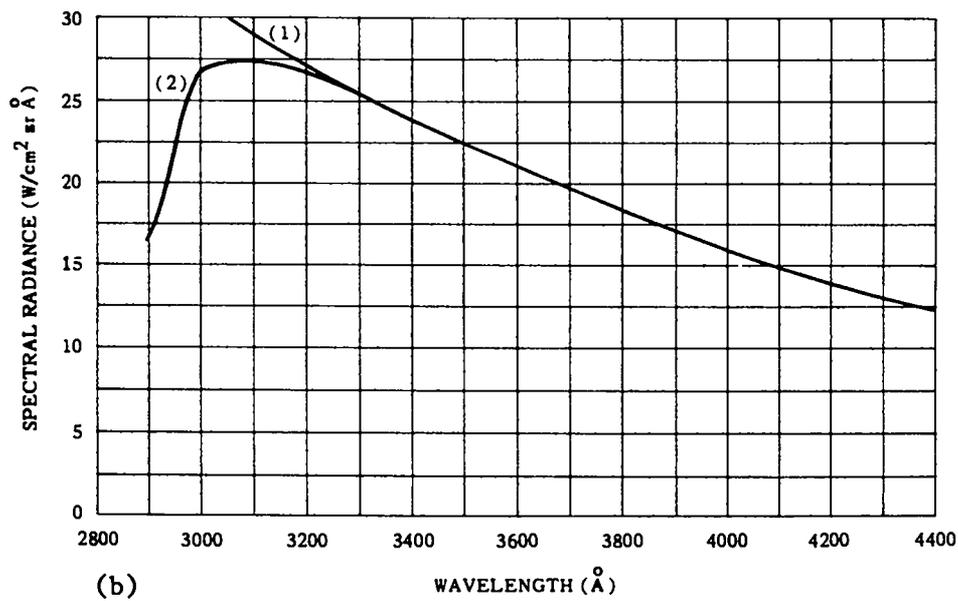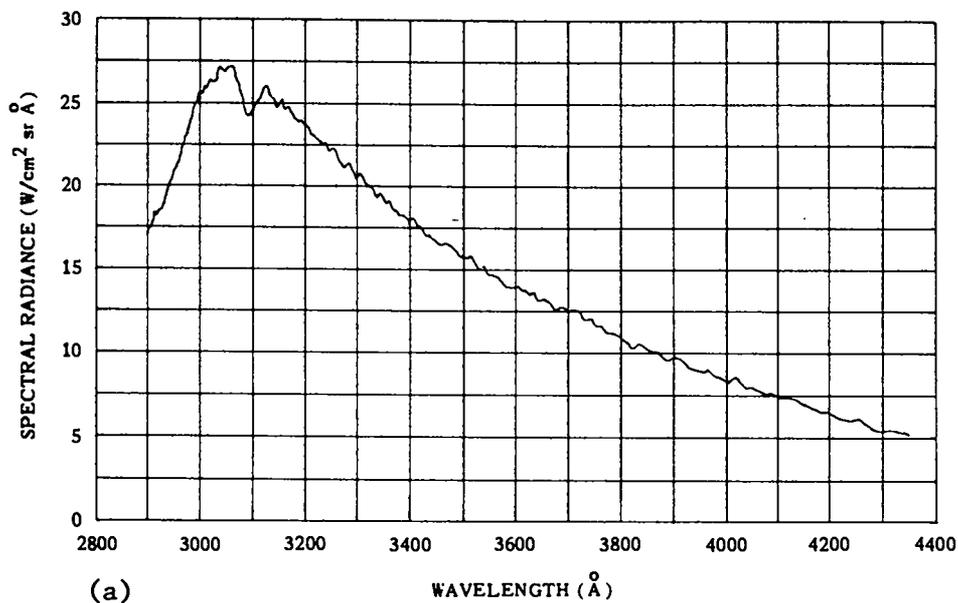
Fig. 5. (a) Spectral radiance of argon flash lamp vs wavelength 0.5 µs before detonation. (b) Spectral radiance of a 17000 K blackbody (1) bare, and (2) as seen through a column of ozone containing 6×10^{17} molec/cm^2 of O_3.
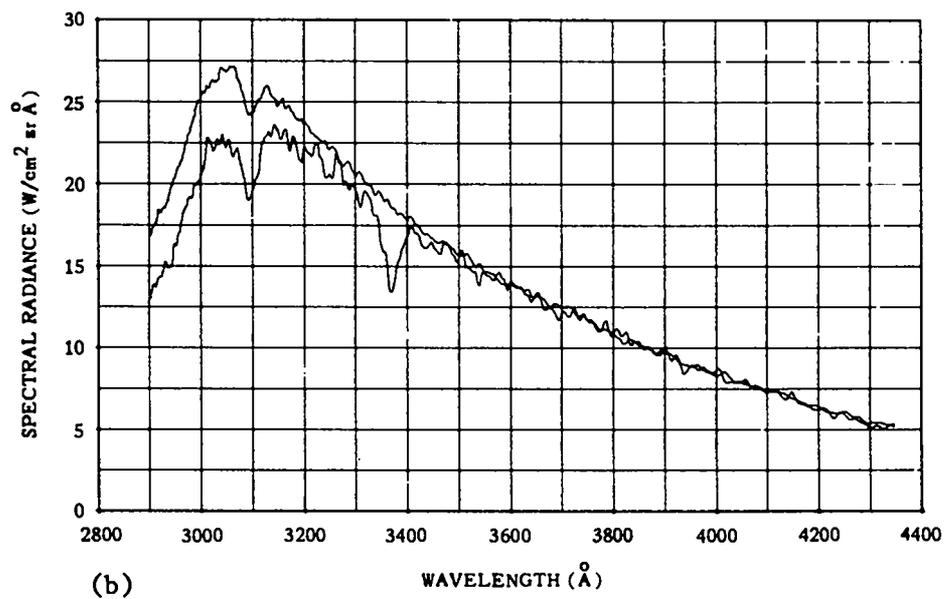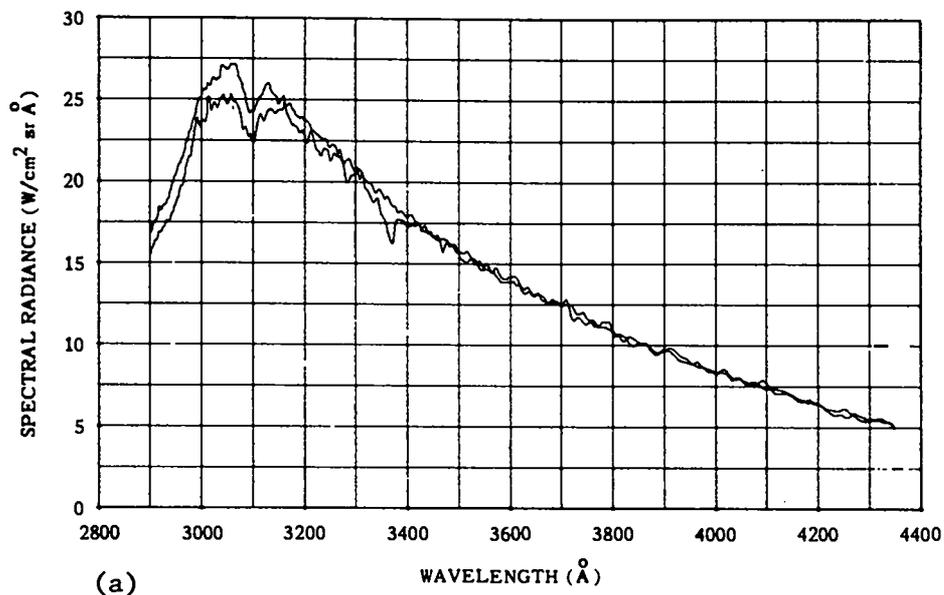
Fig. 6. (a) Spectral radiance of argon lamp vs wavelength before dosing (upper curve) and at 1.96 μs detector time (lower curve). (b) Spectral radiance of argon lamp vs wavelength before dosing (upper curve) and at 4.01 μs detector time (lower curve).

10
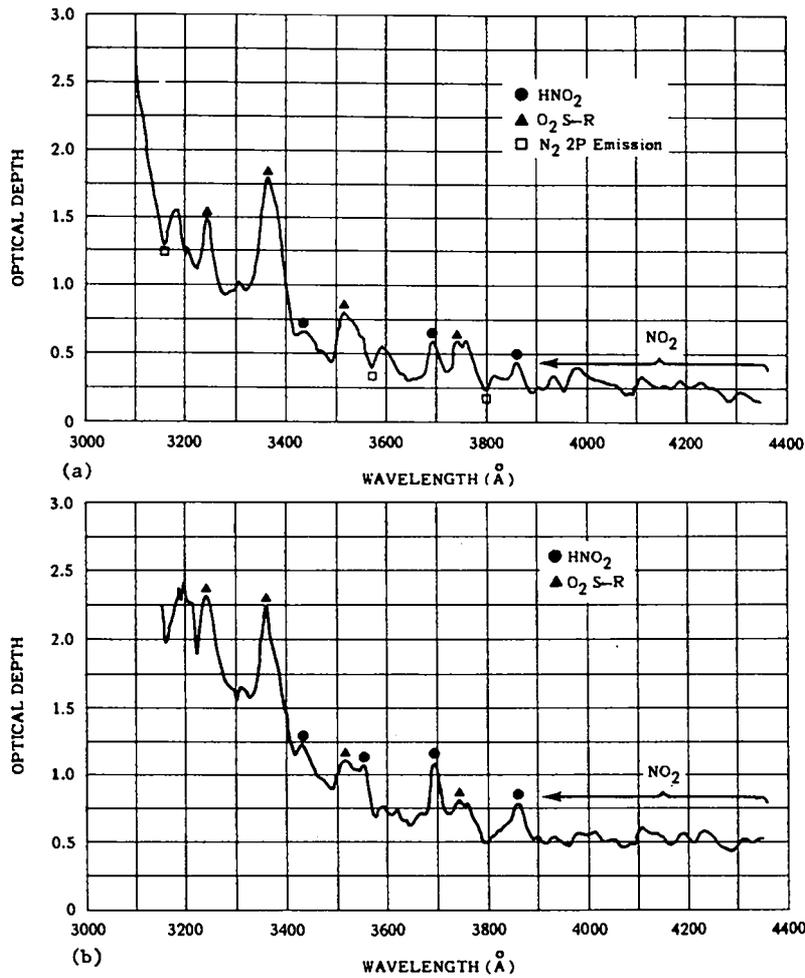
Fig. 7.   (a) Optical depth vs wavelength, Navajo chord at 7.92 μs.   (b) Optical depth vs wavelength, Navajo chord at 15.15 μs.
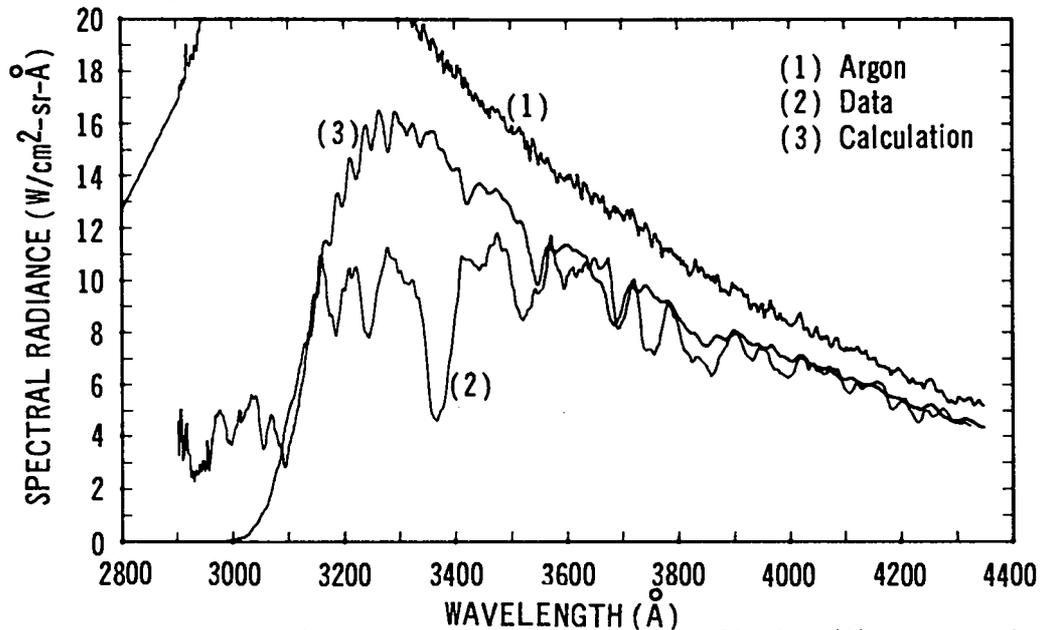
Fig. 8.   A composite of (1) spectrum of the argon flash; (2) measured   spectrum at 7 μs; (3) computer-generated synthetic spectrum representing the argon flash attenuated by 2.19×10^{18} molec/cm^2 of HNO$_2$, 2.7×10^{17} molec/cm^2 of NO$_2$ and 1.7×10^{19} molec/cm^2 of O$_3$.   (Navajo)

11

things have been left out of the synthetic spectrum, notably the O_2^* Schumann-Runge bands. In addition to the O_2^* bands, there appears to be some unaccounted-for continuum absorption at 3150 Å to 3550 Å. We speculate that this may be the O_2 Broida-Gaydon continuum associated with the expected elevated concentration of $O_2(^1\Sigma)$.

Column densities of several of the vibrationally excited O_2^* populations were derived and reported by Mitchell (EG&G, internal document). The O_2^* are oxygen molecules in the ground $(X^3\Sigma_g^-)$ electronic state, and the observed absorption bands involve excitations to the $B^3\Sigma_u^-$ state (Schumann-Runge system). The measured column densities of O_2^* in several vibrational quantum levels are plotted vs time in Fig. 9. These column densities exhibit no obvious relationship to the energy deposition integrals in Fig. 2.

The O_2^* Schumann-Runge bands have been seen in many other nuclear tests, and, in two cases, studied with high spectral resolution, sufficient to identify and assign the component rotation lines.[2] The production and collisional deactivation of O_2^* have also been studied in the laboratory in flash photolysis experiments with O_3.[3,4] O_2^* is known to form in reactions of $O(^3P)$ or $O(^1D)$ with O_3. However, in the case of the Navajo experiment we believe it is formed mainly by electron collisions with O_2 during the initial gamma ray and neutron deposition process.

We have not shown any error bars in Figs. 3 or 4, because there is no clear way of estimating them. The question of the presence or absence of ozone has always been a matter of controversy. No band structure attributed to O_3 has even been seen in fireball or chord spectra--only the rather sharp continuum spectral cutoff at 2900 to 3200 Å, which looks like O_3. After 15 μs the uncertainty of the measured O_3 concentrations is quite large--perhaps ±50%. The uncertainty of NO_2 concentrations could be ± 30%.

III. IVY-KING FIREBALL SPECTRUM

The analysis of fireball spectra is subject to many pitfalls. By contrast with chord spectra, there is no known "reference" spectrum against which the measured spectra can be compared. Moreover, the absorbing species are close to
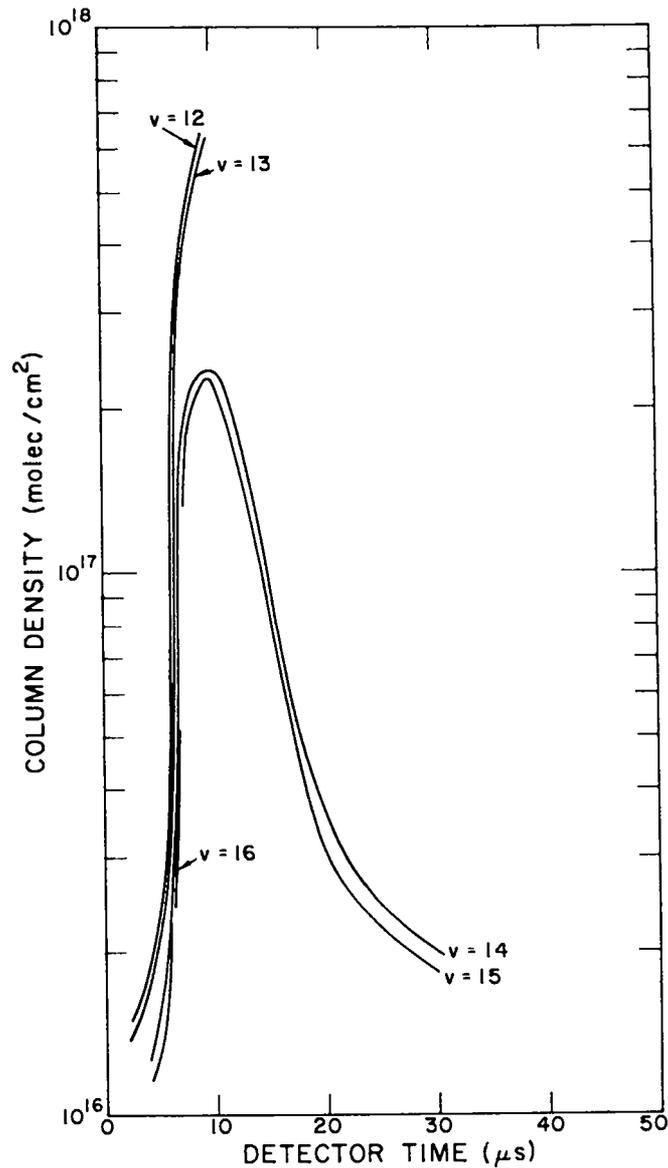
Fig. 9. Measured column densities of five vibrationally excited levels of O_2. (Navajo)

the fireball, and tend to be at elevated temperatures, at least for some of the time.

To obtain absorber column densities from the King spectrum, we assumed that the "bare" fireball radiated as a blackbody, whose temperature was known as a function of time from the measured shock velocities, combined with Rankine-Hugoniot conditions and the air equation of state. This assumption is

probably valid between first maximum and the shoulder at ca. ten times first maximum, which occurs when the shock temperature has dropped to about 0.8 eV. Then, if we are able to measure the <u>absolute</u> spectral intensities on the spectrographic film as functions of time, we can calculate the attenuation factors and the optical thicknesses of absorbers outside the fireball. This requires an accurate radiometric calibration of the film and the spectrograph optical system. Next, if the absorbers are not too strongly heated, so that we have reasonable knowledge of their absorption cross sections, we can infer absorber column densities from the measured optical depths.

In the case of King, this procedure seemed to work out fairly well. Some results are shown in Figs. 10 through 15. Each of the figures consists of (1) a measured spectrum, from radiometric reduction of the film record, at some particular time, and (2) a computer-generated synthetic spectrum, representing a blackbody, whose temperature corresponds to the measured shock velocity, attenuated by an assumed mixture of absorber species. In each case the assumed column densities of absorbers are those that appear to give the best fit to the measured spectrum. The species included in the synthetic spectra are O_3, HNO_2, "cold" NO_2, and "hot" NO_2. Cold NO_2 has absorption cross sections characteristic of room temperature NO_2; the "hot" NO_2 is assumed to have cross sections characteristic of 2000 K.

Figure 10 compares the measured and synthetic spectra at 2.1 to 4.3 ms. The shock temperature ("bare" fireball brightness temperature) would have been about 49000 K at that time. The synthetic spectrum at this time fits the data rather well, with the indicated amounts of O_3, HNO_2, and cold NO_2. No hot NO_2 appeared to be necessary. Part of the 49000 K blackbody spectrum is also shown, and one may note that the smog attenuation is quite large—especially in the blue.

Figure 11 is a similar presentation for the interval 4.3 to 6.4 ms. The shock temperature at this time was about 23000 K. Again the fit is rather good and no hot NO_2 seems to be required. The quality of the fit is least good in the red end beyond 5000 Å, for unknown reasons.

14
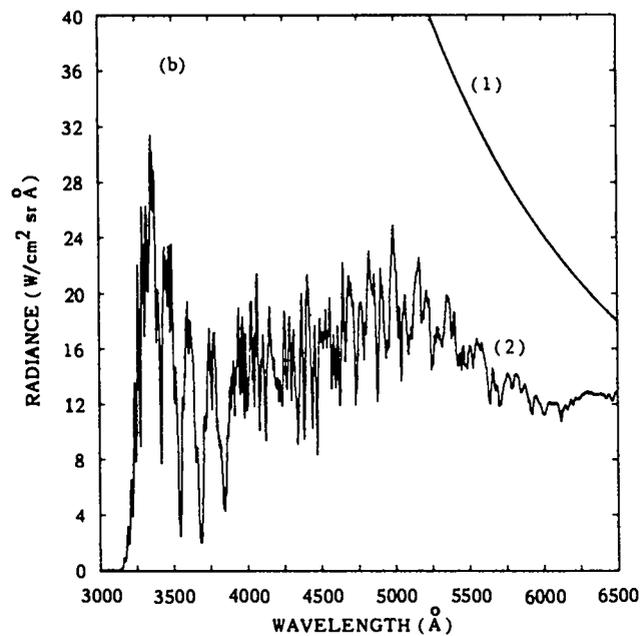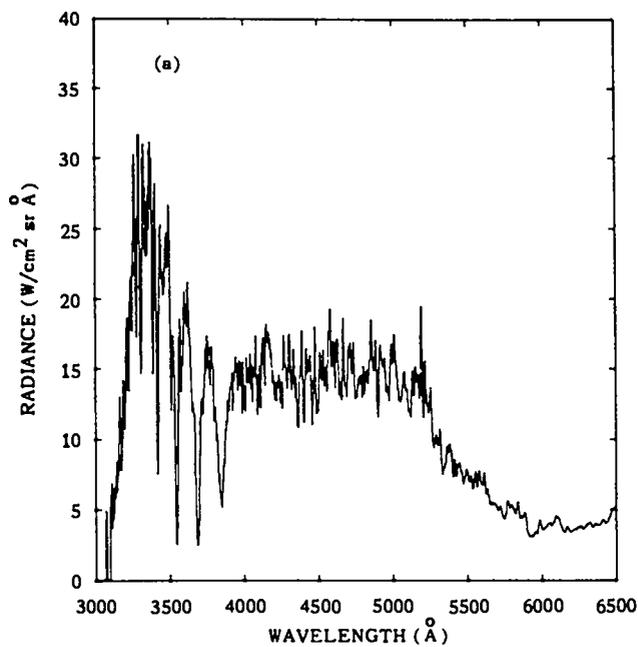
Fig. 10.
Ivy-King fireball brightness at 2.1 to 4.3 ms; (a) data and (b) calculated. The calculated curves include a blackbody at 49000 K (1) bare and (2) as seen through 2.0×10^{19} molec/cm^2 of HNO$_2$ plus 3.0×10^{18} molec/cm^2 of NO$_2$ plus 1.2×10^{20} molec/cm^2 of O$_3$.
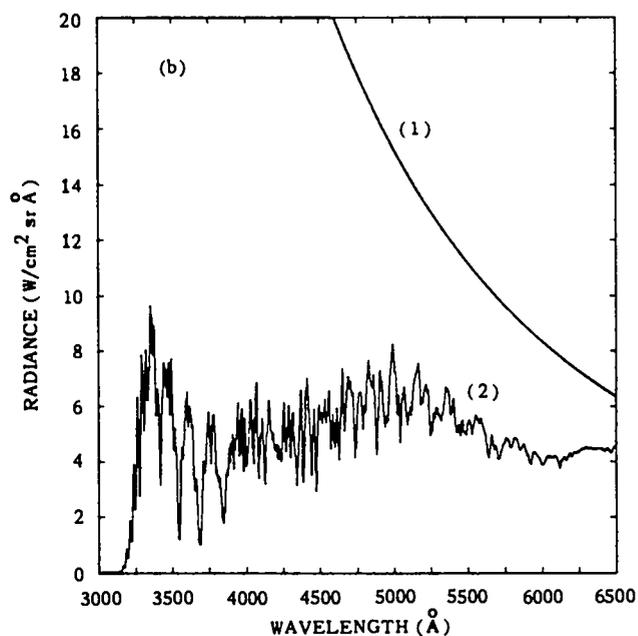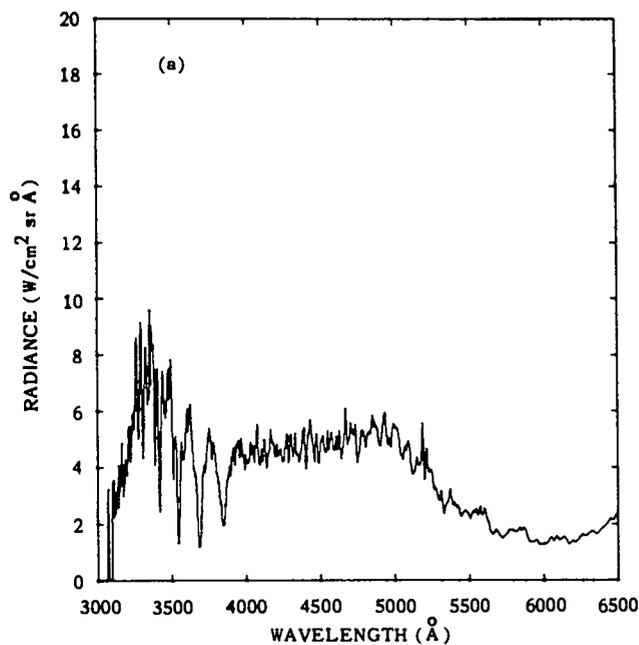
Fig. 11.
Ivy-King fireball brightness at 4.3 to 6.4 ms; (a) data and (b) calculated. The calculated curves include a blackbody at 23000 K (1) bare and (2) as seen through 1.6×10^{19} molec/cm^2 of HNO$_2$ plus 2.8×10^{18} molec/cm^2 of NO$_2$ plus 1.2×10^{20} molec/cm^2 of O$_3$.

15
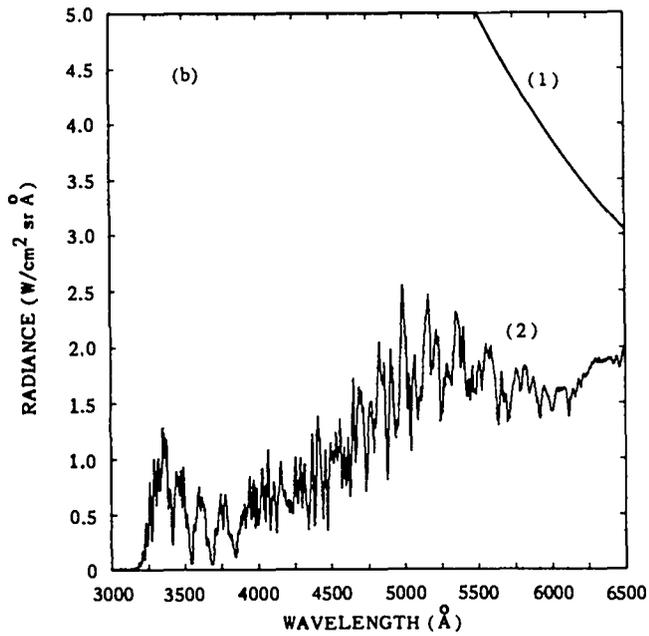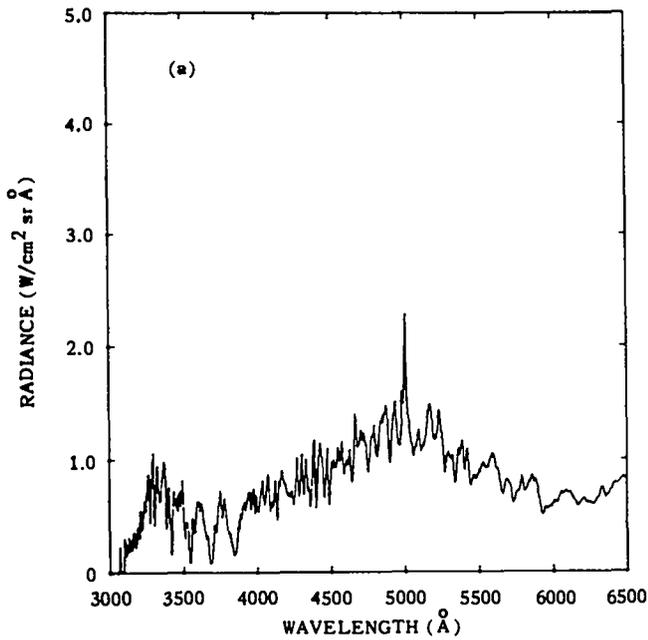
Fig. 12.

Ivy-King fireball brightness at 6.4 to 8.6 ms; (a) data and (b) calculated. The calculated curves include a blackbody at 15000 K (1) bare and (2) as seen through 2.5×10^{19} molec/cm^2 of HNO$_2$ plus 4.5×10^{18} molec/cm^2 of NO$_2$ plus 1.5×10^{20} molec/cm^2 of O$_3$.

Fig. 13.

Ivy-King fireball brightness at 10.7 to 12.9 ms; (a) data and (b) calculated. The calculated curve is of a blackbody at 10000 K as seen through 3.0×10^{19} molec/cm^2 of HNO$_2$ plus 6.0×10^{18} molec/cm^2 of NO$_2$ plus 1.5×10^{20} molec/cm^2 of O$_3$.

16

Fig. 14.

Ivy-King fireball brightness at 20.9 ms; (a) data and (b) calculated. The calculated curve is of a blackbody at 7000 K as seen through 3.0×10^{19} molec/cm^2 of HNO_2 plus 5.6×10^{18} molec/cm^2 of NO_2 plus 1.2×10^{20} molec/cm^2 of O_3 plus 3.0×10^{18} hot molec/cm^2 of NO_2.

Fig. 15.

Ivy-King fireball brightness at 42.4 ms; (a) data and (b) calculated. The calculated curves include a blackbody at 4000 K (1) bare and (2) as seen through 3.0×10^{19} molec/cm^2 of HNO_2 plus 4.5×10^{18} molec/cm^2 of NO_2 plus 1.0×10^{20} molec/cm^2 of O_3 plus 3.0×10^{20} molec/cm^2 of hot NO_2.

17

Figure 12 is a similar presentation for the interval 6.4 to 8.6 ms, when the shock temperature was 15000 K. The same comments apply as for Figs. 10 and 11. The apparent emission feature at 5000 Å is a scratch on the film.

Figure 13 is the same thing at 10.7 to 12.9 ms. Still no hot NO_2 is indicated.

Figure 14 is at 20.9 ms. At this time the shock temperature should have decreased to 7000 K, at which point it is no longer fully opaque. Now a considerable amount of hot NO_2 is indicated, and the quality of the fit between the synthetic spectrum and the data are no longer very good. Our method of analysis begins to fail at this point because the "fireball" is no longer so clearly defined, with no definite radius or definite temperature. Moreover the NO_2 and other absorbers outside the source have a broad range of temperatures.

Figure 15 is a similar presentation at 42.4 ms. Now the shock temperature has dropped to 4000 K, and all the same statements apply as for Fig. 14.

The aggregate of results are summarized in Fig. 16, in which the inferred column densities of each of the absorber species are plotted vs time. The assumed shock temperatures are also plotted.

IV. COMPUTER MODEL

A. General Structure

The computer model is basically RADFLO Lagrangian hydrodynamics with multigroup radiation transport in spherical symmetry (Refs. 5, 6) with add-ons for gamma ray and neutron energy deposition and for chemistry. The photoabsorption coefficients, which in RADFLO are normally generated from tables based on assumptions of local thermodynamic and chemical equilibrium, are modified in this model according to the computed departures from equilibrium, wherever the temperature is below 5000 K. Chemical equilibrium concentrations are computed in all mesh cells, irrespective of their temperature. The chemical rate equations are integrated only in mesh cells in which T < 5000 K. In those cells the differences between the chemical species
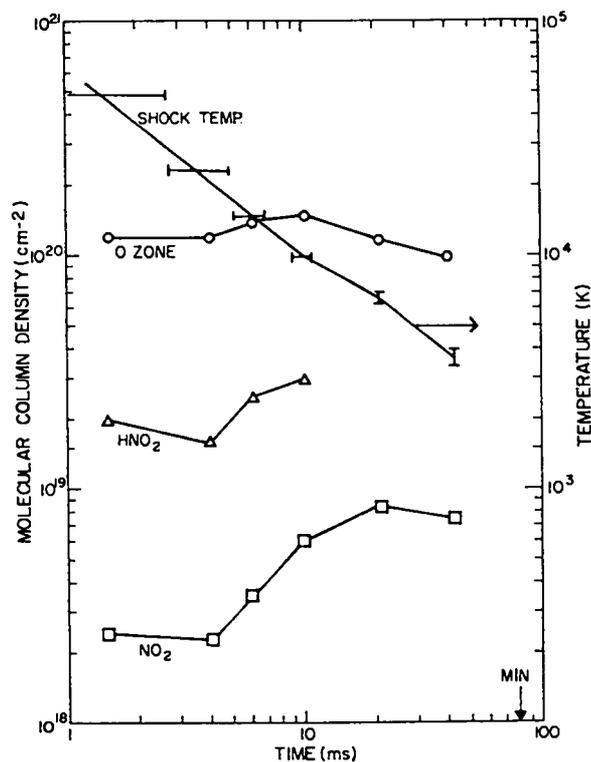
18

Fig. 16. Column densities of O_3, HNO_2, and NO_2 as inferred from the Ivy-King spectrum. Also shown are the shock temperatures derived from the radius-time data.

concentrations computed with the rate equations and those computed for chemical equilibrium are used to correct the radiative absorption coefficients generated with the LTE tables for the departures from chemical equilibrium. This requires a separate set of tabulations of absorption cross sections of each chemical species for each RADFLO frequency group.

The chemical rate coefficients in each mesh cell are recomputed at frequent intervals to take account of changes in temperature. Chemical species concentrations are adjusted for hydrodynamic expansion and compression in addition to the chemical rate processes. Photodissociation, photoionization, and metastable photoexcitation rate coefficients in each cell are computed from the computed radiation fluxes convolved with the tabulated photochemical cross sections. For certain chemical species additional source terms are included to account for production by neutrons, gammas, and x rays.

19

B. Chemistry Sub-Model

The chemical model ordinarily includes 22 chemical species. For special purposes we use an expanded chemistry model, which includes the same 22 species plus $O_2(^1\Sigma)$, O_3^* (metastable excited ozone), and four quantum-level groups of O_2^*. The six new species were added in an attempt to represent a feature that we have called the "ozone photochemical precursor." The complete species list and the reaction rate parameters are tabulated in Appendix A. The ion chemistry model is simplified by combining the vast number of possible ion species into a small number of classes, and using averaged reaction rate coefficients for each of the ion classes. There are two positive ion classes, which we call "Air$^+$" and "H_3O^+," and two negative ion classes, which we call "O_2^-" and "NO_2^-." "Air$^+$" is a composite of the short-lived ion species N_2^+, O_2^+, N^+, and O^+ in the proportions 0.63/0.16/0.14/0.07. Air$^+$ ions are created initially by the ionizing radiation, and they tend to engage in reactions that convert them to the more stable H_3O^+. Likewise O_2^- is the initial negative ion, formed by attachment of electrons to O_2, and subject to easy photodetachment. It reacts to form the more stable negative ion NO_2^-. The ion chemistry is described in more detail in Appendix A.

The neutral species set is rather complete, and all known reactions are included which connect different members of the set.

The absorption of ionizing radiation in air produces, for each 35 eV of energy, approximately one ion-pair, 0.3 $O(^3P)$ and $O(^1D)$ atoms, 0.3 $N(^4S)$ atoms, 0.4 $N(^2D)$ atoms, and many excited N_2 and O_2 molecules. The $N(^2D)$ reacts rapidly with O_2 to form NO and more $O(^1D)$. The ions are mostly N_2^+ and O_2^+, along with some N^+ and O^+.

During the prompt gamma ionization pulse not too far from the bomb, the ion and electron densities become very large – as high as 10^{14} cm^{-3} or so. When the ion-electron densities exceed 10^{14} cm^{-3} the fastest reactions are 3-body 2-electron recombination reactions, such as

$$N_2^+ + e^- + e^- \rightarrow N_2 + e^- \quad . \tag{R1}$$

20

Some additional N and O atoms may be formed in these reactions. During the neutron deposition phase, or farther from the bomb, the ion-electron densities are substantially smaller than 10^{14} cm^{-3}. Under those circumstances the ions and electrons tend to react with neutrals, rather than with one-another. There are many possible reactions, but they tend to convert the original positive ions to the more stable species NO^+, H_3O^+, and their hydrates. The electrons attach to O_2 to form O_2^-. In the formation of H_3O^+, one OH radical is usually formed, along with some HNO_2. In the eventual recombination of H_3O^+ with electrons or O_2^-, one H atom is formed. The H quickly attaches to O_2 to make HO_2. The net result is that approximately one OH radical and one HO_2 radical are formed for each original ion pair, almost irrespective of the amount of water vapor initially present in the air (within reason). The OH and HO_2 are powerful oxidizers, and they are the main agents for converting the copious N atoms to NO. They also react with NO to form NO_2, HNO_2, and HNO_3.

Additional details of the generic ion chemistry model are discussed in Appendix A. It is noted that the rate coefficients for two generic reaction paths that lead to stable hydrated ions (H_3O^+ and NO^+H_2O) from less stable transient ions (O_2^+ and NO^+) are unknown. Those two reactions are very important because they also control the rate of production of OH radicals, H atoms, and some of the HNO_2. We have had to set the rate coefficients for those two reactions on the basis of the Navajo data. Therefore it should not seem amazing that the computations fit those data rather well. It is more amazing that the same model, with the two rate coefficients fitted to Navajo, should then give a good fit to the fireball spectral data from King. The same model furthermore generates optical and infrared radiant power vs time curves which, for large yield fireballs, are in substantial agreement with observational data.

The most important optical absorber in fireball smog is NO_2. However, NO_2 is a very minor constituent of the smog, compared to such species as O_3, NO, OH, and HO_2. The latter species are transparent to visible light, and hard to detect spectroscopically. The NO_2 is also subject to rapid photodissociation by light from the fireball, and its concentration is often determined by a photochemical equilibrium between the production reactions

$$NO + HO_2 \rightarrow NO_2 + OH \tag{R2}$$

and

$$NO + O_3 \rightarrow NO_2 + O_2 \tag{R3}$$

and the photochemical destruction

$$NO_2 + h\nu \rightarrow NO + O . \tag{R4}$$

Therefore, to compute NO_2 concentrations correctly, one must be careful in treating the mutual interaction between the NO_2 and the optical radiation.

Ozone also tends to be photodissociated by radiation from the fireball, in the near ultraviolet. The O_3 photodissocation leads to the possibility, close to the fireball, of a rather exotic set of photochemical and optical pumping reactions that can, in effect, catalyse the photodissociation of O_2 and enhance the odd-oxygen concentration. We have called this the "ozone photochemical precursor," believing that it may help to explain the anomalously low brightness of a low yield fireball at first maximum. The essential notion is that O_2 is extremely opaque for wavelengths shorter than 1800 Å, the Schumann-Runge photodissociation threshold; therefore essentially no photons of shorter wavelengths, which can dissociate O_2, exist outside the fireball where O_2 is present. On the other hand, the vibrationally excited species O_2^* can be dissociated by photons with wavelengths longer than 1800 Å—i.e., outside of the fireball. Therefore, O_2^* can be important for the odd-oxygen balance—i.e., for the concentrations of O_3, NO_2, HO_2, and O outside of the fireball. Because of the potential importance of the O_2^*, we have attempted to include it in our chemical model in some detail, despite the fact that the O_2^* vibrational quantum levels are far out of Boltzmann equilibrium.

We use the term O_2^* to represent the aggregate of vibrational quantum levels $v > 1$, but the precise value of v is of course important. The higher the quantum number, in general, the longer will be the threshold wavelength for

22

photodissociation, and the larger the photodissociation rate outside the fireball. O_2^* in vibrational levels up to $v = 27$ is known to be formed in the reaction[3,4]

$$0 + O_3 \rightarrow O_2^* + O_2^* \; . \tag{R5}$$

["O" without other identifier is intended to mean ground state $O(^3P)$.] The reactions

$$O(^1D) + O_3 \rightarrow \begin{cases} O_2^* + O + O & \text{(R6)} \\ O_2^* + O_2^* & \text{(R7)} \end{cases}$$

produce vibrational excitations up through the dissociation continuum, with $v = 30$ being the highest observed. These reactions tend to occur wherever O_3 is being photodissociated. Close to the fireball the main O_3 photodissociation reaction is

$$O_3 + h\nu \; (\lambda \leqslant 3090 \; \text{Å}) \rightarrow O(^1D) + O_2(^1\Delta) \; . \tag{R8}$$
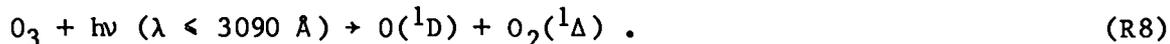
The $O(^1D)$ engages in reactions R6 and R7, but more often it reacts with O_2 via

$$O(^1D) + O_2 \rightarrow 0 + O_2(^1\Sigma) \; . \tag{R9}$$

We think that we may see the Broida-Gaydon continuum of $O_2(^1\Sigma)$ in the Navajo chord spectrum. We also see O_2^* in levels up through $v = 16$. The concentrations of O_2^* are so large that it appears to be necessary to assume that in Navajo O_2^* is made mainly by direct electron excitation of O_2 during the deposition of neutrons and gamma rays.

$$O_2 + e \rightarrow O_2^* + e \; . \tag{R10}$$

O_2^* is deexcited to lower O_2^* levels by collisions with O, O_3, and other molecules. The rates of deexcitation by O and O_3 have been inferred from experiments by Webster and Bair,[4] but rates of deexcitation by O_2 and N_2 have not been measured. In our computer model we have treated the rate of collisional deexcitation of O_2^* by O_2 and N_2 as an adjustable parameter. From comparison of the computed results with the Navajo data, we find that the adjustable rate must be much smaller than the measured rates of deexcitation by either O or O_3.

Close to the fireball the higher levels of O_2^* can be populated by optical pumping from lower O_2^* levels. Schumann-Runge band absorptions by O_2^* in low vibrational levels produce excitations to the $B^3\Sigma_u^-$ state, which are followed rapidly by emission (and/or collisional quenching) transitions back to various vibrational levels of the ground $X^3\Sigma_g^-$ state. Because of the relative alignment of the potential curves for the B and X states (see Fig. 17) the final vibrational levels tend to be higher than the initial ones. The reverse can also occur--that is Schumann-Runge absorptions from high-lying O_2^* states can be followed by emissions to lower O_2^* states. These processes, taken together with the collisional deexcitation processes, can tend to produce quasi-equilibrium vibrational state distributions which are characterized by a temperature that is somewhere between the local radiation temperature and the material temperature.

We have attempted to include the above processes in our chemistry model. Because of computing constraints it was unfeasible to include all possible O_2 vibrational levels as distinct chemical species; so we have, instead, identified five groups of vibrational levels, viz:

"O_2": $v = 1$

"$O_2^*(V1)$": $2 < v < 5$

"$O_2^*(V2)$": $6 < v < 9$

"$O_2^*(V3)$": $10 < v < 18$

"$O_2^*(V4)$": $v > 18$
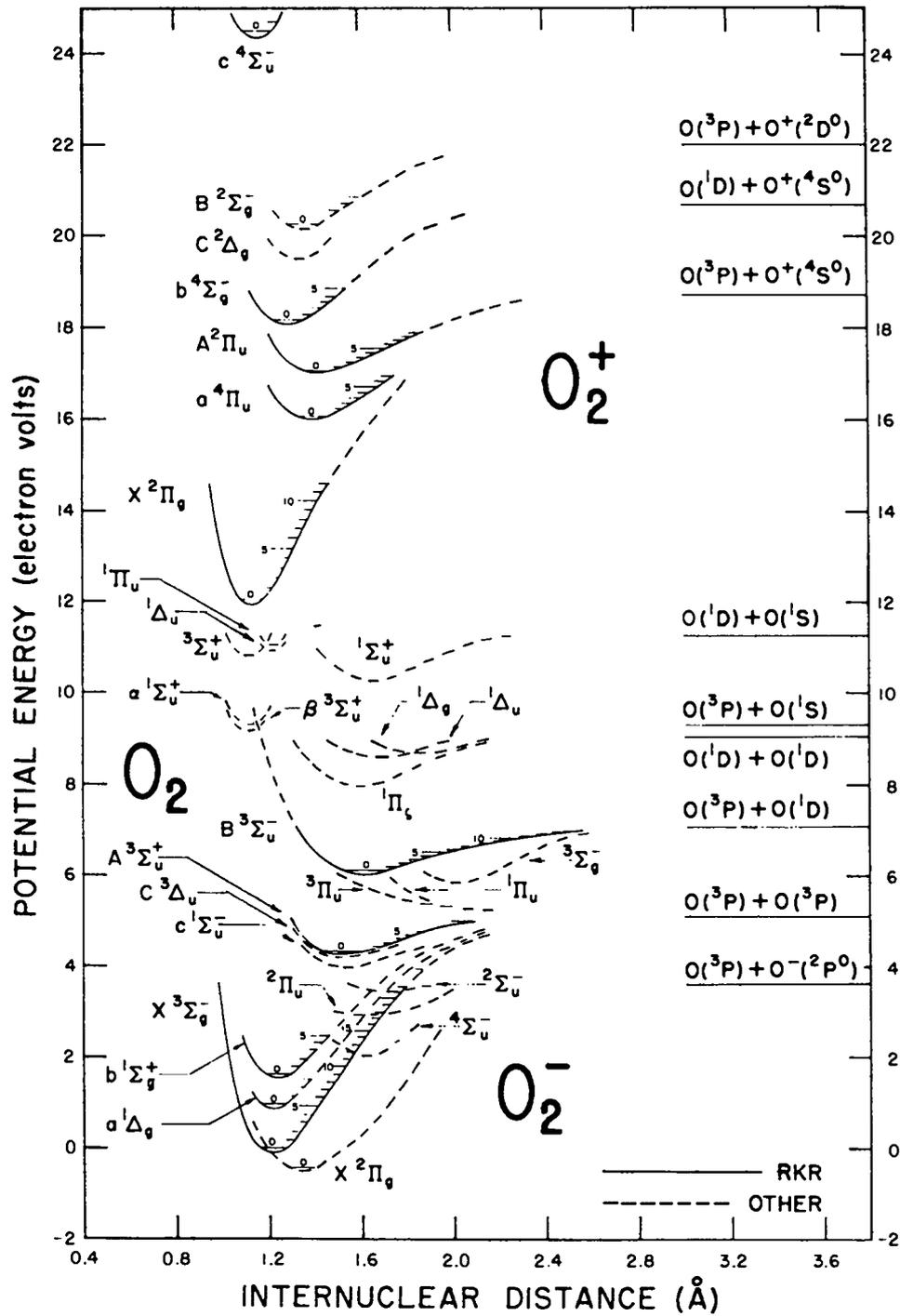
Fig. 17. Potential energy curves for O_2^-, O_2 and O_2^+ (from Krupenie[7]).

Using band intensities and Franck–Condon factors tabulated by Krupenie[7] and additional Franck–Condon factors computed by Mitchell,[8] we have attempted to compute photochemical rate coefficients for photodissociation of each of the O_2^* species and optical pumping transitions from each one to each other. We have had to assume some of the predissociation probabilities as well as the continuum cross sections for absorptions to the unbound $^3\Pi_u$ state (fully allowed).

The inclusion of these processes leads to increased column densities of all odd–oxygen species, compared to the column densities that would be computed otherwise. This leads to an increased attenuation of optical and infrared emission fom low yield fireballs at first maximum, though not yet as much as the data suggest. The computed amounts of O_2^* are reasonably in line with observations, both for Navajo and for low yield fireballs. However, we have had to guess at several rate parameters and cross sections. These include the production efficiencies of O_2^* by neutrons and gamma rays, the collisional deexcitation coefficients for O_2^* on O_2 and N_2, several predissociation probabilities, and the continuum photoabsorption cross sections for $^3\Pi_u - X^3\Sigma_g^-$ and the $A^3\Sigma_u^+ - b^1\Sigma_g^+$ Broida–Gaydon systems.

C. Neutron and Gamma Ray Sub-Models

The model assumes spherical symmetry.

The prompt gamma ray deposition at distance R from the bomb begins at time R/c and ends at time $R/c + \tau_\gamma$. During this interval the gamma energy deposition rate is assumed to be constant, and given by the expression

$$\dot{E}_\gamma = \frac{f_\gamma \kappa Y}{4\pi R^2 \tau_\gamma} \exp(-\kappa \rho R) \quad \text{erg/g·s} , \tag{1}$$

where f_γ is the fraction of the bomb yield Y (in ergs) radiated in gamma rays, and κ is the average gamma mass absorption coefficient (cm^2/g).

The neutron deposition has two rather distinct components – one associated with the initial kinetic energy of the neutrons, and the other associated with the energy released in neutron (n,p) and (n,γ) capture reactions with $_7N^{14}$ nuclei. The total neutron kinetic energy is f_nY, where f_n is the neutron kinetic-energy-yield fraction. The total (n,p) and (n,γ) energy released is about $1.8 \times 10^{-6}N_n$ ergs, where N_n is the total number of neutrons emitted by the bomb, and where we have assumed that the rate-weighted average energy released by the (n,p) and (n,γ) capture reactions is 1.1 MeV.

We assume that the radial distribution of neutron energy deposition is described by the function

$$F_R(R) = \frac{3}{2} \frac{e^{-R/\lambda}}{4\pi R^2 \lambda} \quad cm^{-3} \quad , \tag{2}$$

where

$$\lambda = \lambda_0 (\frac{\lambda_0}{R})^{1/2}(\frac{\rho_0}{\rho})^{3/2} \quad , \tag{3}$$

The volume integral of $4\pi R^2 F(R)dR$ from zero to infinity is 1. The value of λ_0 fitted to the Monte Carlo computations is 4×10^4 cm. Normally $\kappa = .0113$ cm^2/g and $\tau_\gamma = 10^{-7}$ s. τ_γ represents the gamma straggling time due to scattering.

We assume the neutron energy deposition rate in erg/g.s can be represented by

$$\dot{E}_n(R,t) = (F_R/\rho)[f_nYF_1(t)+ 1.47 \times 10^{-6}N_nF_2(t)] \quad , \tag{4}$$

where $F_1(t)$ and $F_2(t)$ are normalized rates for neutron kinetic energy deposition and capture reactions, respectively.

$$F_1(t) = (1/\tau_1) \exp\left\{(t - R/v_n)/\tau_1\right\} \quad s^{-1} \tag{5}$$

and

$$F_2 = (1/\tau_2) \exp\left\{t-R/v_n)/\tau_2\right\} \quad s^{-1} \tag{6}$$

The value of τ_2, based on measured thermal neutron (n,p) cross sections, is 0.047 s. For Navajo, the values of v_n and τ_1, fitted to the Monte Carlo computations are 5×10^9 cm/s and 10^{-5} seconds, respectively. For King we assume $v_n = 3.4 \times 10^8$ cm/s and $\tau_1 = 1.5 \times 10^{-4}$ s.

For fission product decay gammas

$$\dot{E}_{\gamma d} = .027 \; \dot{Y}_\gamma T_\gamma / 4\pi R^2 \quad erg/g \cdot s \quad , \tag{7}$$

where

$$T_\gamma = \exp\left\{-.027 \int_o^R \rho \, dr\right\} \tag{8}$$

and

$$\dot{Y}_\gamma = .0089 \; f_f Y \left[\frac{1}{t+100} + \exp\left\{-.012(3 + \log_{10}t)^4\right\}\right] \quad erg/s. \tag{9}$$

The $\dot{Y}_\gamma$ expression is appropriate for U_{238} fission products.[9]

To model the Navajo chord experiment the values chosen for the neutron and gamma ray fractions f_n and f_γ were those that best fit the results of the 3-D Monte Carlo computations of the time integrals of the neutron and gamma deposition rates along the chord. The Monte Carlo results showed pronounced shadowing effects--i.e., pronounced asymmetries in the neutron and gamma ray deposition on the chord, compared to what would be expected for a spherically symmetric source, and what we compute with our spherical algorithm.

28

D. Retarded-Time Integrals

To compute column integrals of computed chemical species concentrations along a chord, for comparison with experimental data, as in the Navajo chord experiment, it is necessary to account properly for the finite velocity of light. The same is true for the chord integrals of the computed density of gamma/neutron energy deposition. Computing the time-retarded integrals requires some special manipulations. Light that reaches the detector at a detector time t from a point on the chord at distance L from the detector originated at or passed by that point at an earlier time $t - L/c$. If the detector is at distance R_D from the bomb and the point in question is at distance R from the bomb and the distance of the chord from the bomb is R_C, then L is given by

$$L = \sqrt{R_D^2 - R_C^2} - \sqrt{R^2 - R_C^2} \quad . \tag{10}$$

Zero-time at the detector is later than zero-time at the bomb by the amount R_D/c. The "time-retarded" chord-integral of a quantity q at a bomb-time t (or detector time $t - R_D/c$) is

$$Q(t) = \int_o^{L_{max}} q\{R,(t - \frac{R + L}{c})\} \, dL \quad , \tag{11}$$

where the bracket means functional dependence. The quantity q refers to either computed chemical species concentrations or radiation energy deposited. To compute the chord integrals Q(t) we need to form sums of the quantities $q\Delta L$ computed for different mesh cell radii R at times that are earlier than t by the amounts $(R + L)/c$. This is done by storing tables of the computed quantities q for the entire mesh at each of a number of bomb-times t. The integrals Q are evaluated from these tables by interpolating in the time domain.

V. MODEL RESULTS FOR NAVAJO

We began by adjusting the gamma and neutron yield fractions f_γ and f_n so that the values of the chord integrals agreed with the 3-D Monte Carlo results after essentially all of the gammas and neutrons were deposited. Then we ran the model and computed, among other things, the (time-retarded) chord integrals of the energy deposited as a function of detector time. The result is plotted in Fig. 18 along with the 3-D Monte Carlo result (from Fig. 2), which it was
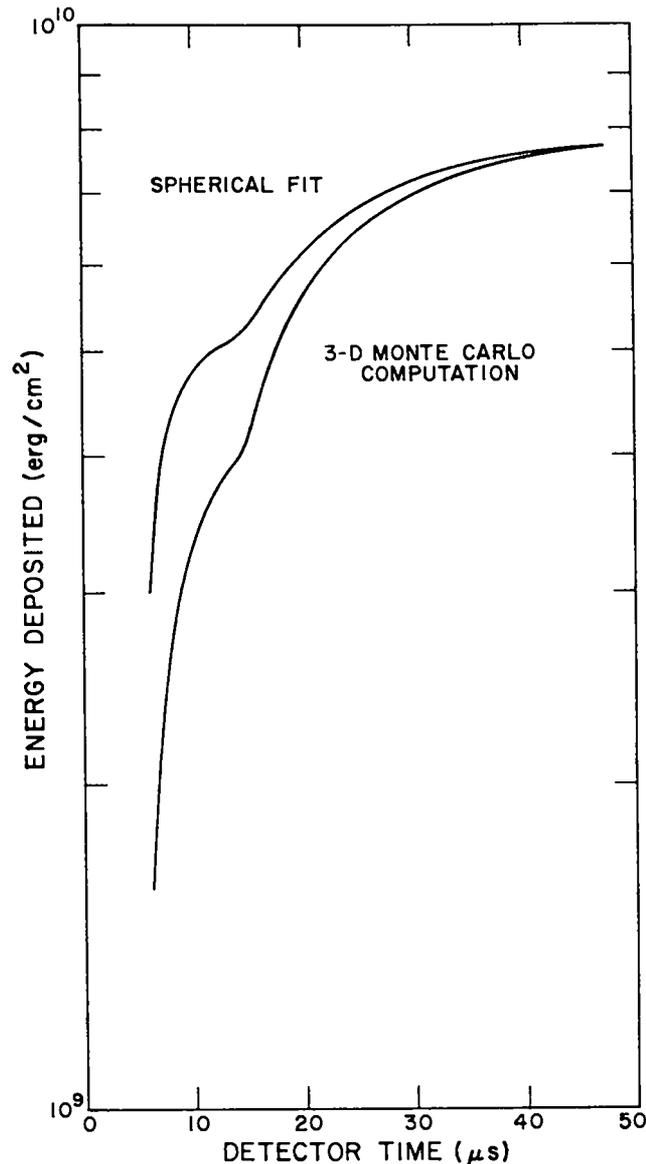
Fig. 18. Time-retarded path integrals of gamma ray and neutron energy deposition along Navajo chord (1) 3-D Monte Carlo computations (2) spherical fit by Eqs. (1) through (11).

intended to approximate. It is clear from the comparison that the spherical model is a poor approximation to the real 3-D situation. This need not bother us too much if the quantities of interest are mainly the production efficiencies of absorbing species (molecules per erg). The computed time-retarded chord integrals of the concentrations of O_3, NO_2, and HNO_2 are plotted vs detector time in Fig. 19. They are to be compared with the data in Fig. 3. The computed production efficiencies (molecules per erg, or molecules per ion pair) are plotted in Fig. 20, along with the data, replotted from Fig. 4.

The computed chord integral of the concentration of $O_2^*(V3)$ is plotted vs detector time in Fig. 21. Since this species represents the aggregate of 9 vibrational quantum states, we should expect this chord integral to be approximately 9 times as large as the corresponding integral for just one of those states. If we compare Fig. 21 with the measured chord integrals for levels 12 through 16 in Fig. 9, we see a vague correspondence.

The computer model generates large quantities of $O_2(^1\Sigma)$, also plotted in Fig. 21. The computed $O_2(^1\Sigma)$ chord integral at 7 μs is 1.7×10^{19} molec/cm^2. The large amount of $O_2(^1\Sigma)$ may explain the otherwise mysterious absorption at 3200 to 3500 Å seen in the 7-μs spectrum in Fig. 8.

From a theoretical point of view, Navajo was a clean and simple case. The thermal radiation transport, hydrodynamics, and photochemical reactions were of no importance on the time scale of the experiment, and the air along the chord was not appreciably heated. Therefore the data furnish an excellent baseline calibration of our model. In fact, as noted earlier, we have used the data to evaluate two ion reaction rate coefficients, as well as the collisional deexcitation coefficients for O_2^*.

VI. MODEL RESULTS FOR IVY-KING

For the King computer simulation we assumed values of gamma ray and neutron yield fractions based on detailed device output computations. We used
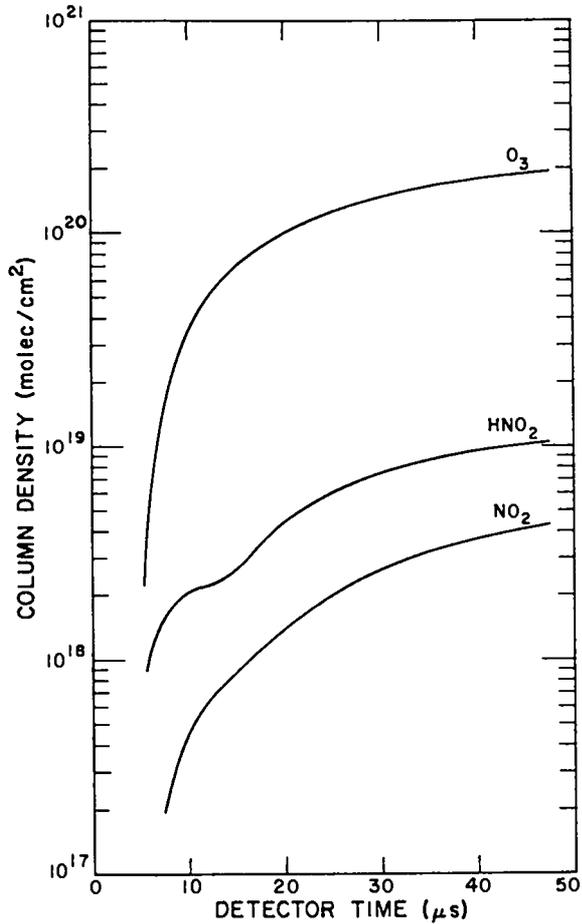
Fig. 19.
Time-retarded chord integrals of the computed concentrations of O_3, HNO_2, and O_3. (Navajo)
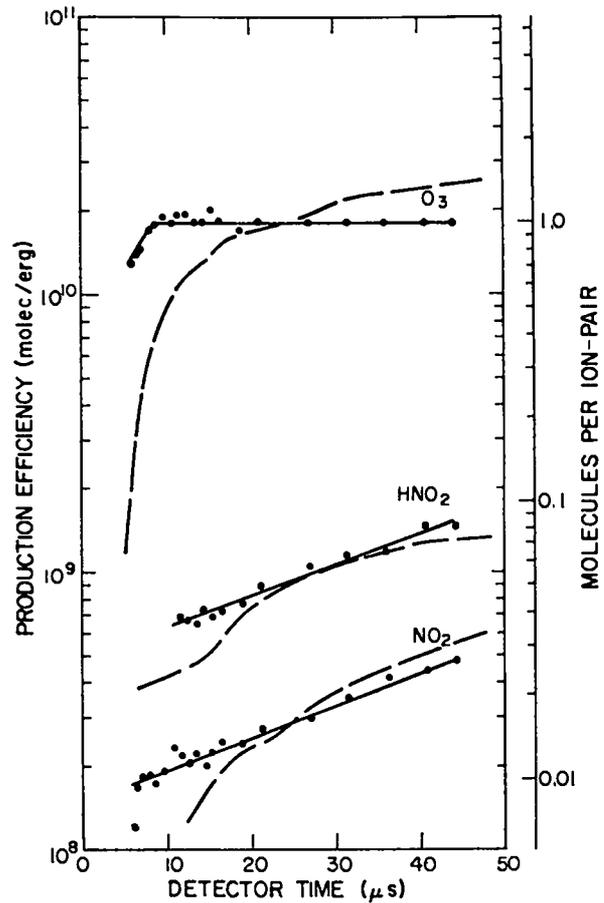
Fig. 20.
Production efficiencies or O_3, HNO_2 and NO_2 vs detector time. Solid lines and points are experimental data (see Fig. 4). The dashed curves are computed with the model. (Navajo)

the same initial production efficiencies for O, $O(^1D)$, N, and $N(^2D)$ as were assumed for Navajo. The King explosion was about 500 kt.

The results, in terms of computed column densities of O_3, NO_2, and HNO_2 from the fireball surface to infinity, are shown in Fig. 22, along with the data, replotted from Fig. 15. The computations agree with the data quite well with no further adjustments of parameters.

From the King data analysis (Figs. 10 through 15) we concluded that the NO_2 was effectively cold before 20 ms and partially hot thereafter. This observation is in agreement with the computer model results. The computer also shows that the ozone is effectively cold up to and somewhat past minimum time. This kind of information can be useful in the analysis of fireball spectra where an absolute radiometric calibration is not available. When the NO_2 and O_3 are known to be cold, then the detailed spectral structure of their absorption cross sections can be utilized for differential analysis.

VII. COMPUTATION FOR A GENERIC 1-Mt EXPLOSION

Figure 23 is a computed radiant power vs time curve for a generic one-megaton explosion. The spectral bandpass is that of an unfiltered silicon photodetector. The nuclear device was arbitrarily assumed to have a gamma ray yield fraction of 0.3% and a neutron fraction of 0.8%. The computed radiant power at first maximum is only 14% as large as the power that was computed for an identical device without the nonequilibrium chemistry (smog) effects included.[5]

The extra power-time curve shown as a dashed line is a computer-generated estimate of the additional radiant power due to neutron-induced fluorescence. The fluorescence power is assumed to be proportional to the column integral of the ion-pair production rate, with an assumed effective fluorescence efficiency of 1×10^{-5}. The fluorescence decay time is τ_1 (see Eq. 5), which was assumed to be 10^{-5} s.

Fig. 21. Computed chord column densities of O_2^* (V3) and $O_2(^1\Sigma)$ vs detector time. (Navajo)

Fig. 22. Column densities of O_3, HNO_2, and NO_2 from the King event. Solid curves and points are experimental (see Fig. 16). Dashed curves are computed with the model.

Fig. 23. Computed radiant power vs time curve for a generic 1-Mt explosion as convolved with the spectral response function of a bare silicon detector. Dashed curve represents neutron-induced flourescence signal.

ACKNOWLEDGMENTS

APPENDIX A

CHEMISTRY/PHOTOCHEMISTRY

We will refer to two separate chemistry models. The first, called Model A, includes 22 species. Model B has six additional species, all metastable excited states of O_2 and O_3. The chemical species included in the Model A are:

N_2, O_2, H_2O, N, O, H, $O(^1D)$, NO, OH, NO_2, HO_2, O_3, HNO_2, NO_3, HNO_3, H_2O_2, N_2O_5, e^-, Air^+, H_3O^+, O_2^-, NO_2^-, where the species Air^+, H_3O^+, O_2^- and NO_2^- represent generic ion classes.

The additional species included in Model B are

$$O_2(^1\Sigma), \quad O_2^*(V1), \quad O_2^*(V2), \quad O_2^*(V3), \quad O_2^*(V4), \quad O_3(\alpha).$$
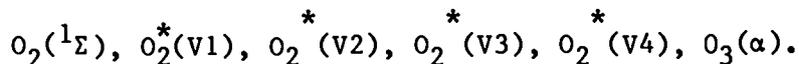
Table A-I is a computer listing of the chemical reactions and rate parameters used in model A, along with source references.

With the exception of photon reactions and mutual neutralization reactions, all of the rate coefficients are expressed in the form

$$k = A(T/300)^B \exp{-C/T}.$$

The parameters A, B, and C are listed for each reaction.

For photochemical reactions the rates are computed interactively from cross sections and computed spectral fluxes convolved over 42 wavelength bands. For these reactions no rate parameters are listed in the table.

For ion-ion mutual neutralization reactions, where we have used the generic rate coefficients from the DNA Reaction Rate Handbook,[10] the effective two-body rate coefficients are assumed to be of the form

$$k = A(T/300)^B + C(T/300)^{B-2}[M] .$$

For these reactions the entry in column C is a number in parentheses, to distinguish it from an activation energy.

For certain three-body reactions there is a limiting concentration of the moderator, [M], above which [M] does not matter. That limiting value of [M] is given in parentheses.

Some of the rate parameters in Table I-A are estimates. Most of these are flagged with the word "estimate" in the reference column. Some of the other reactions are indicated as "reverse." In each of those cases the rate coeffficient has been computed from the known or published rate of the opposite reaction divided by the computed equilibrium constant.

Many of the ion reactions in Table I-A will seem strange. They are based on the following reasoning. According to Myers and Schoonover,[1] at 60 km the initial mix of positive ion species produced per initial ion-electron pair are: 0.626 N_2^+, 0.159 O_2^+, 0.14 N^+, and 0.075 O^+O. Initially "Air$^+$" is assumed to consist of this mixture of species. Consequently, when it engages in reactions of the type Air$^+$ + e$^-$ + e$^-$ $\rightarrow$ neutral product + e$^-$, with the generic rate coefficient of $7 \times 10^{-20}(T/300)^{-4.5}$ cm^{6}s^{-1} (from the DNA Reaction Rate Handbook), the neutral products are assumed to be N_2, O_2, N, or O, with the relative probabilities 0.626, 0.159, 0.14, and 0.075.

The reactions $Air^+ + e^- \rightarrow$ products are assumed to include only the dissociative recombination reactions

$$N_2^+ + e^- \rightarrow N + N(^2D) \quad \left(k=1.8 \times 10^{-7}(T/300)^{-.4}\right)$$

and

$$O_2^+ + e^- \rightarrow O + O(^1D) \quad \left(k=2.1 \times 10^{-7}(T/300)^{-.6}\right) .$$
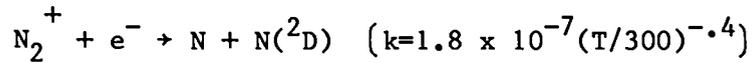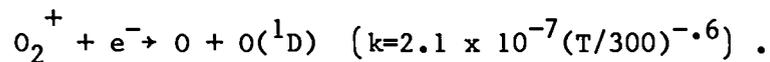
The first of these is assumed to be followed immediately by the reaction

$$N(^2D) + O_2 \rightarrow NO + O(^1D)$$
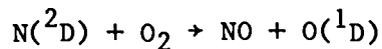
irrespective of the O_2 concentration. In the model, this sequence is represented by two $Air^+ + e^-$ reactions, namely

$$Air^+ + e^- \rightarrow N + NO + O, \quad \left(k = 1.13 \times 10^{-7}(T/300)^{-.4}\right),$$

and

$$Air^+ + e^- \rightarrow O + O(^1D) \quad \left(k = 3.3 \times 10^{-8}(T/300)^{-.6}\right).$$
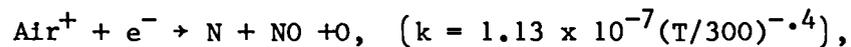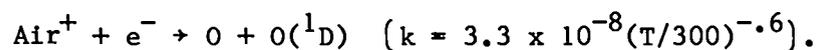
The effect of these reactions on the molecular O_2 concentration is ignored.

The preceding reactions will dominate when the ion density is large – i.e. greater than about 10^{14} cm^{-3}. With lower ion concentrations the fastest ion reactions will be reactions with neutrals to produce more stable ion forms,

38

such as H_3O^+ and NO^+ hydrates. Initially the N_2^+ ions charge exchange with O_2 to form O_2^+. The N^+ ions also charge exchange with O_2 along two paths namely

$$N^+ + O_2 \rightarrow O_2^+ + N$$
$$N^+ + O_2 \rightarrow NO^+ + O$$
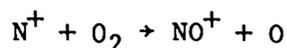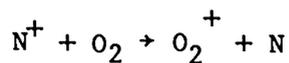
with very equal rates. Thus, after a very short time the mix of positive ion species is changed to 0.93 O_2^+ and 0.07 NO^+, along with the production of about 0.15 additional O atoms and 0.07 additional N atoms. These extra N and O atoms are conveniently ignored in comparison with the larger number of N and O atoms formed in the initial ionization process.

The O_2^+ and NO^+ ions engage subsequently in an involved sequence of reactions with water to form H_3O^+, $NO^+ \cdot H_2O$, and higher hydrates. In the process a substantial amount of OH is formed, along with a small amount of HNO_2. The most important reactions are

$$O_2^+ + H_2O + M \rightarrow O_2^+ \cdot H_2O + M \left(k = 1.9 \times 10^{-28} (T/300)^{-1} \right)$$

$$O_2^+ \cdot H_2O + H_2O \rightarrow H_3O^+ + OH + O_2 \left(k = 2 \times 10^{-10} \right)$$

We represent these reactions schematically as

$$Air^+ + 2H_2O \rightarrow H_3O^+ + OH + O_2 \quad .$$
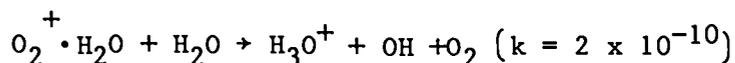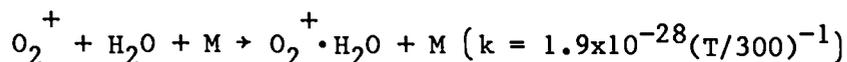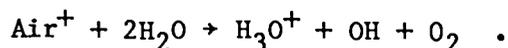
This reaction is very important, because it is the main source of OH radicals and ultimately, upon neutralization of the H_3O^+ ions, the main source of H and HO_2. However, its rate is very uncertain. In the absence of other

information we have fitted the rate coefficient based on the Navajo data. The rate coefficient that we obtained is 1×10^{-27} cm^6/s.

Another important sequence is

$$NO^+ + H_2O + M \rightarrow NO^+ \cdot H_2O + M$$

$$NO^+ \cdot H_2O + H_2O + M \rightarrow NO^+ \cdot (H_2O)_2 + M$$

$$NO^+ \cdot (H_2O)_2 + H_2O \rightarrow H_3O^+ \cdot H_2O + HNO_2 \quad .$$

We represent these reactions schematically as

$$Air^+ + H_2O + H_2O \rightarrow H_3O^+ + HNO_2,$$
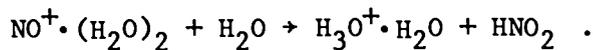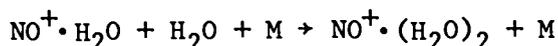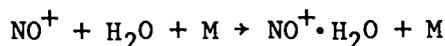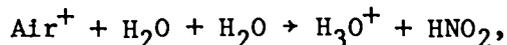
where again the rate coefficient is unknown. We find that to fit the Navajo data we must assume $k \simeq 1 \times 10^{-27}$ cm^6/s.

In the mutual neutralization reactions between Air^+ and O_2^- and between Air^+ and NO_2^- we assume that Air^+ is comprised of 0.93 parts O_2^+ and 0.07 parts NO^+, and the reaction rates are prorated accordingly. In neutralization reactions of the generic species H_3O^+, we assume the products are those corresponding to neutralization of real H_3O^+, namely $H + H_2O$.

Table A-II is a listing of the additional reactions that are included in chemistry Model B. This model includes many more guessed rate coefficients than model A , and is therefore less reliable. Some of the guessed rate coefficients are based on some relevant published information, and in those cases the source is indicated with an asterisk.

The chemical rate equations are integrated only for mesh cells where the temperature is below 5000 K. At higher temperatures we assume that chemical equilibrium exists. The equilibrium concentrations are computed as described in Appendix B. When the temperature of a cell is decreasing and drops below 5000 K the equilibrium concentration is used to set the initial conditions for the subsequent chemical rate problem.

For the T < 5000 K regime the chemical reaction set is balanced, in the sense that a reverse reaction is included for every given reaction. In all cases the ratios of the forward and reverse rate coefficients are equal to the equilibrium constants.

THE CHEMICAL REACTIONS
Model A

Reactants			Products			A	B	C	References
N	OH		NO	H		5.30E-11	0.0	0.	Hampson[11]
NO2	H		NO	OH		1.20E-09	0.0	971.	Anderson,[12]
N	HO2		NO	OH		2.00E-11	0.0	0.	Bortner[10]
O	HNO2		OH	NO2		1.00E-12	0.0	0.	Estimate
NO	HO2		NO2	OH		3.40E-12	0.0	-250.	DeMore[13]
O	HNO3		OH	NO3		3.00E-17	0.0	0.	Hampson[11]
HO2	NO2		HNO2	O2		3.00E-15	0.0	0.	Hampson[11]
O	OH		O2	H		4.00E-11	0.0	0.	DeMore[13]
O	HO2		OH	O2		3.50E-11	0.0	0.	DeMore[13]
H	O3		OH	O2		1.40E-10	0.0	470.	DeMore[13]
OH	O3		HO2	O2		1.60E-12	0.0	940.	DeMore[13]
HO2	O3		OH	O2	O2	1.10E-14	0.0	580.	DeMore[13]
H2O2	NO		OH	HNO2		1.60E-18	0.0	1040.	Hampson[11]
OH	HNO2		NO2	H2O		6.60E-12	0.0	0.	Hampson[11]
OH	HNO3		H2O	NO3		1.52E-14	0.0	-644.	Marinelli and Johnston[14]
NO	NO2	H2O	HNO2	HNO2		6.00E-38	0.0	0.	Hampson[11]
N2O5	H2O		HNO3	HNO3		1.00E-20	0.0	0.	Hampson[11]
O(1D)	H2O		OH	OH		2.30E-10	0.0	0.	DeMore[13]
H	HO2		H2O	O		8.30E-11	0.0	500.	Hampson[11]
H	HO2		OH	OH		4.20E-10	0.0	950.	Hampson[11]
OH	OH		H2O	O		1.00E-11	0.0	500.	DeMore[13]
O(1D)	H2O2		OH	HO2		5.20E-10	0.0	0.	Hampson[11]
O	H2O2		OH	HO2		2.80E-12	0.0	2125.	DeMore[13]
OH	HO2		H2O	O2		1.16E-10	0.0	0.	Hochanadel et al.[15]
HO2	HO2		H2O2	O2		2.50E-12	0.0	0.	DeMore[13]
H	H2O2		OH	H2O		2.90E-12	0.0	1400.	Hampson[11]
OH	H2O2		H2O	HO2		1.00E-11	0.0	750.	DeMore[13]
N	O2		NO	O		4.40E-12	0.0	3220.	DeMore[13]
O(1D)	NO2		NO	O2		1.00E-10	0.0	0.	Hampson[11]
O	NO2		NO	O2		9.30E-12	0.0	0.	DeMore[13]
N	O3		NO	O2		1.00E-15	0.0	0.	DeMore[13]
O	NO3		O2	NO2		1.00E-11	0.0	0.	DeMore[13]
O3	NO		NO2	O2		2.30E-12	0.0	1450.	DeMore[13]
NO2	O3		NO3	O2		1.20E-13	0.0	2450.	DeMore[13]
N	NO		N2	O		3.40E-11	0.0	0.	DeMore[13]
N	NO2		NO	NO		7.00E-13	0.0	0.	Estimate
N	NO2		N2	O2		7.00E-13	0.0	0.	Estimate
NO	O2	NO	NO2	NO2		3.30E-39	0.0	-530.	Hampson[11]
NO	NO3		NO2	NO2		1.90E-11	0.0	0.	Hampson[11]
NO3	NO3		NO2	NO2	O2	5.00E-12	0.0	3000.	Hampson[11]
O(1D)	O3		O2	O2		6.60E-12	0.0	0.	DeMore[13]
O(1D)	O3		O2	O	O	1.20E-10	0.0	0.	DeMore[13]
O	O3		O2	O2		1.50E-11	0.0	2118.	DeMore[13]
NO	H		N	OH		2.46E-10	-.2	24548.	Reverse
NO	OH		N	HO2		4.89E-12	.1	43988.	Reverse
NO	OH		NO2	H		9.97E-12	.4	15772.	Reverse
NO2	OH		NO	HO2		2.15E-11	-.2	4389.	Reverse
OH	NO2		O	HNO2		1.81E-13	.5	12179.	Reverse
HNO2	O2		HO2	NO2		1.72E-14	-.4	15668.	Reverse
OH	NO3		O	HNO3		1.02E-17	.2	682.	Reverse
O	OH		H	O2		1.53E-15	0.0	3187.	Reverse
O2	H		O	OH		7.96E-11	-.2	8407.	Reverse
OH	O2		H	O3		1.68E-12	.6	39229.	Reverse
OH	O2		O	HO2		3.78E-11	.1	27847.	Reverse
HO2	O2		OH	O3		3.56E-13	.4	20259.	Reverse
OH	O2	O2	HO2	O3		2.85E-40	.5	16224.	Reverse
NO2	H2O		OH	HNO2		7.98E-12	.6	20639.	Reverse
OH	HNO2		H2O2	NO		7.15E-18	-.3	0.	Reverse
H2O	NO3		OH	HNO3		1.97E-13	.3	9143.	Reverse
HNO2	HNO2		NO	NO2	H2O	1.05E-11	-1.1	3343.	Reverse
HNO3	HNO3		N2O5	H2O		3.33E-21	1.0	3855.	Reverse
H2O	O		OH	OH		6.22E-11	.1	8960.	Reverse

Reactants			Products			A	B	C	References
OH	OH		H	HO2		2.17E-11	.3	20390.	Reverse
H2O	O		H	HO2		2.89E-11	.4	28400.	Reverse
OH	OH		O(1D)	H2O		2.31E-11	-.2	14357.	Reverse
H2O	O2		OH	HO2		7.91E-10	.2	36307.	Reverse
OH	HO2		O	H2O2		3.72E-13	.3	8626.	Reverse
OH	HO2		O(1D)	H2O2		4.63E-11	.3	29318.	Reverse
H2O2	O2		HO2	HO2		2.04E-11	-.3	21346.	Reverse
OH	H2O		H	H2O2		1.33E-13	.7	35801.	Reverse
H2O	HO2		OH	H2O2		8.53E-12	.4	15711.	Reverse
NO	O		N	O2		1.01E-12	0.0	19361.	Reverse
NO	O2		N	O3		5.63E-17	.5	63308.	Reverse
NO	O2		O	NO2		1.60E-12	.2	23208.	Reverse
NO	O2		O(1D)	NO2		1.15E-11	.2	46025.	Reverse
NO2	O2		O3	NO		3.25E-12	.2	25408.	Reverse
O2	NO2		O	NO3		1.76E-13	.8	34689.	Reverse
NO3	O2		NO2	O3		1.64E-12	-.3	14928.	Reverse
N2	O		N	NO		1.26E-10	.1	37736.	Reverse
NO2	NO2		NO	NO3		1.95E-12	.5	11480.	Reverse
NO2	NO2		NO	O2	NO	8.41E-13	-.3	12423.	Reverse
NO2	NO2	O2	NO3	NO3		1.34E-40	1.5	13007.	Reverse
O2	O2		O	O3		3.68E-12	.5	49385.	Reverse
O2	O	O	O(1D)	O3		2.05E-36	.3	10614.	Reverse
O2	O2		O(1D)	O3		1.98E-11	.4	69983.	Reverse
N	O	O	NO	O		3.00E-33	0.0	0.	Bortner[10]
O	O	N2	O2	N2		4.80E-33	0.0	0.	Hampson[11]
O	N	N2	NO	N2		1.04E-32	-.5	0.	Hampson[11]
O	NO	N2	NO2	N2		1.55E-32	0.0	-584.	Hampson[11]
N	N	N2	N2	N2		8.30E-34	0.0	-500.	Hampson[11]
O	O	O	O2	O		1.40E-30	0.0	650.	Bortner[10]
O	O	O2	O2	O2		3.00E-33	0.0	0.	Bortner[10]
OH	NO	M	HNO2	M	(4.5E19)	1.66E-32	0.0	-1110.	DeMore[13]
H	NO2	M	HNO2	M		5.00E-31	-2.4	0.	Bortner[10]
OH	NO2	M	HNO3	M	(9.2E18)	6.43E-32	0.0	-1110.	DeMore[13]
HO2	NO	M	HNO3	M		3.30E-33	0.0	0.	Crutzen[16]
O	H	M	OH	M		2.00E-32	0.0	0.	Hampson[11]
H	O2	M	HO2	M		2.09E-32	0.0	-290.	DeMore[13]
O	OH	M	HO2	M		1.00E-31	0.0	0.	Bortner[10]
H	OH	M	H2O	M		6.78E-31	-2.0	0.	Hampson[11]
OH	OH	M	H2O2	M	(1.2E20)	2.50E-31	-.8	0.	DeMore[13]
NO2	O	M	NO3	M		1.00E-31	0.0	0.	Hampson[11]
NO	O2	M	NO3	M		1.00E-40	0.0	0.	Bortner[10]
NO3	NO2	M	N2O5	M	(1.3E18)	2.80E-30	0.0	0.	Hampson[11]
O	O2	M	O3	M		1.13E-34	0.0	-510.	DeMore[13]
NO	O2	NO2	NO3	NO2		3.06E-40	1.0	0.	Reverse
O	O2	O2	O3	O2		6.93E-37	-.0	6346.	Reverse
NO3	NO2		NO	O2	NO2	1.11E-12	0.0	1473.	Hampson[11]
O2	N2		O	O	N2	3.95E-08	.1	59370.	Reverse
NO	N2		O	N	N2	2.03E-08	-.4	75511.	Reverse
NO2	N2		O	NO	N2	7.13E-07	-.1	35577.	Reverse
N2	N2		N	N	N2	6.04E-09	.2	112746.	Reverse
HNO2	M	(4.5E19)	OH	NO	M	3.57E-06	-.5	22872.	Reverse
HNO2	M		H	NO2	M	1.04E-06	-2.6	38783.	Reverse
HNO3	M	(9.2E18)	OH	NO2	M	6.53E-05	-.8	22889.	Reverse
HNO3	M		HO2	NO	M	2.18E-05	-.9	28638.	Reverse
OH	M		O	H	M	8.50E-09	.3	50962.	Reverse
HO2	M		H	O2	M	7.81E-09	.3	22825.	Reverse
HO2	M		O	OH	M	7.13E-07	.1	31523.	Reverse
H2O	M		H	OH	M	1.72E-06	-1.6	59423.	Reverse
H2O2	M	(1.2E20)	OH	OH	M	1.25E-05	-1.0	25022.	Reverse
NO3	M		NO2	O	M	4.36E-05	-.6	24681.	Reverse
NO3	M		NO	O2	M	2.41E-13	-.8	1473.	Reverse
N2O5	M	(1.3E18)	NO3	NO2	M	3.66E-03	-2.1	11002.	Reverse
O3	M		O	O2	M	3.77E-09	-.3	11693.	Reverse
O	N		NO			1.90E-17	-.4	0.	Bortner[10]
O	NO		NO2			8.00E-17	-2.0	0.	Bortner[10]
N	N		N2			1.00E-17	-.9	0.	Bortner[10]
O	O		O2			2.00E-17	0.0	12000.	Bortner[10]
O	O		O2			2.40E-21	0.0	0.	Bortner[10]

Reactants			Products			A	B	C	References
O(1D)			O	+ hv		6.80E-03	0.0	0.	Bortner[10]
e	O(1D)		e	O		7.80E-09	-.1	3993.	Bortner[10]
O(1D)	N2		O	N2		2.00E-11	0.0	-107.	DeMore[13]
O(1D)	O2		O	O2		2.90E-11	0.0	-67.	DeMore[13]
e	O		e	O(1D)		5.25E-09	-.2	26810.	Reverse
O	N2		O(1D)	N2		1.35E-11	-.1	22710.	Reverse
e	NO2		NO2-			1.00E-17	0.0	0.	Bortner[10]
e	O2		O2-			2.00E-19	0.0	0.	Bortner[10]
e	NO2		NO2-			4.00E-11	0.0	0.	Bortner[10]
e	O2	M	O2-	M		4.60E-31	0.0	0.	Bortner[10]
e	O2	O2	O2-	O2		1.18E-29	-1.4	6602.	Reverse
e	HNO3		NO2-	OH		5.00E-08	0.0	0.	Bortner[10]
e	HO2		O2-	H		2.29E-05	-1.2	18123.	Reverse
e	NO2		O2-	N		2.01E-04	-1.5	47310.	Reverse
O3	e		O2-	O		3.06E-04	-1.7	7211.	Reverse
e	H2O	H	e	e	H3O+	4.10E-25	-3.2	74715.	Reverse
H	H2O	M	e	H3O+	M	3.52E-32	-1.2	74715.	Reverse
e	e	H3O+	e	H2O	H	7.00E-20	-4.5	0.	Bortner[10]
e	H3O+	M	H	H2O	M	6.00E-27	-2.5	0.	Bortner[10]
e	H3O+		H	H2O		1.30E-06	-.7	0.	Bortner[10]
NO2-	H3O+		H	H2O	NO2	4.00E-07	-.5	(3E-25)	Bortner[10]
O2-	H3O+		H	H2O	O2	4.00E-07	-.5	(3E-25)	Bortner[10]
O2-	M		e	O2	M	7.41E-12	1.4	4992.	Reverse
O2-	H		e	HO2		1.00E-09	0.0	0.	Estimate
O2-	N		e	NO2		3.00E-10	0.0	0.	Bortner[10]
O2-	O		O3	e		1.50E-10	0.0	0.	Bortner[10]
NO2-	OH		e	HNO3		8.67E-16	2.4	3622.	Reverse
O2-	NO2		NO2-	O2		1.20E-09	0.0	0.	Bortner[10]
NO2-	O2		O2-	NO2		2.99E-09	0.0	22629.	Reverse
O2-	HNO2		NO2-	HO2		1.00E-09	0.0	0.	Bortner[10]
NO2-	HO2		O2-	HNO2		4.28E-10	.4	6961.	Reverse
HNO2	+ hv		OH	NO					Johnston and Graham[17]
HNO3	+ hv		OH	NO2					Johnston and Graham[17]
OH	+ hv		O	H					Estimate
HO2	+ hv		OH	O					Garvin[18]
H2O	+ hv		H	OH					Huebner[19]
H2O2	+ hv		OH	OH					Schumb[20]
NO	+ hv		N	O					Park[21]
NO2	+ hv		O	NO					Johnston and Graham[17]
NO2	+ hv		O(1D)	NO					Johnston and Graham[17]
NO3	+ hv		NO2	O					Johnston and Graham[17]
N2	+ hv		N	N					Huebner[19]
N2O5	+ hv		NO2	NO3					Johnston and Graham[17]
O2	+ hv		O	O					Huebner[19]
O2	+ hv		O	O(1D)					Huebner[19]
O3	+ hv		O	O2					Ackerman[22]
O3	+ hv		O2	O(1D)					Ackerman[22]
NO2-	+ hv		e	NO2					Warneck[23]
O2-	+ hv		e	O2					Warneck[23]
Air+	e	e	N2	e		4.38E-20	-4.5	0.	Estimate
Air+	e	e	O2	e		1.13E-20	-4.5	0.	Estimate
Air+	e	e	N	e		9.80E-21	-4.5	0.	Estimate
Air+	e	e	O	e		5.20E-21	-4.5	0.	Estimate
Air+	e		N	NO	O(1D)	1.13E-07	-.4	0.	Estimate
Air+	e		O	O(1D)		3.30E-08	-.6	0.	Estimate
O2-	Air+		NO	O2		2.80E-08	-.5	(3E-25)	Estimate
O2-	Air+		O2	O2		3.90E-07	-.5	(3E-25)	Estimate
NO2-	Air+		NO	NO2		2.80E-08	-.5	(3E-25)	Estimate
NO2-	Air+		O2	NO2		3.90E-07	-.5	(3E-25)	Estimate
Air+	H2O	H2O	H3O+	OH	O2	1.00E-27	0.0	0.	Estimate
Air+	H2O	H2O	H3O+	HNO2		1.00E-27	0.0	0.	Estimate
NO	O2		Air+	O2-		2.00E-07	0.0	100000.	Estimate
NO	O		Air+	O2-		2.00E-07	0.0	90000.	Estimate
HNO2	H2O		H3O+	NO2-		2.19E-07	-.4	85877.	Estimate
HNO3	H2O		H3O+	NO2-		8.83E-08	-.2	82106.	Estimate

THE CHEMICAL REACTIONS
Model B

Reactants			Products			A	B	C	References
H	O3		OH	O2*V3		1.40E-10	0.0	470.	DeMore[13]
H	O3(AL)		OH	O2*V4		1.40E-10	0.0	0.	Estimate
OH	O3		HO2	O2*V1		1.60E-12	0.0	940.	DeMore[13]
OH	O3(AL)		HO2	O2*V2		1.60E-12	0.0	0.	Estimate
O3	NO		NO2	O2*V2		2.30E-12	0.0	1450.	DeMore[13]
O3(AL)	NO		NO2	O2*V3		2.30E-12	0.0	0.	Estimate
O(1D)	O3		O2*V4	O2*V3		1.20E-10	0.0	0.	DeMore[13]
O	O3		O2*V2	O2*V3		1.50E-11	0.0	2118.	DeMore[13]
O	O3(AL)		O2	O2*V3		1.50E-11	0.0	0.	von Rosenberg and Trainor[24]
O	O	M	O2*V3	M		4.80E-33	0.0	0.	Hampson[11]
O	O2	O2	O3(AL)	O2		1.13E-34	0.0	-510.	von Rosenberg and Trainor[24]
O	O2	N2	O3	N2		1.13E-34	0.0	-510.	Hampson[11]
O	O2	O2	O3	O2(SG)		6.93E-37	-.0	6346.	Reverse
O3	O2(SG)		O	O2	O2*V1	2.50E-11	0.0	0.	Bortner[10]
O2(SG)	N2		O	O	N2	1.50E-12	.5	40821.	Reverse
O2(SG)			O2	+ hv		8.30E-02	0.0	0.	Bortner(DNA), 1978
O(1D)	O2		O	O2(SG)		2.90E-11	0.0	-67.	DeMore[13]
O2*V1	O		O2	O		2.20E-12	0.0	0.	Webster and Bair[4]
O2*V2	O		O2	O		2.50E-12	0.0	0.	Webster and Bair[4]
O2*V2	O		O2*V1	O		1.25E-12	0.0	0.	Webster and Bair[4]
O2*V3	O		O2	O		7.00E-12	0.0	0.	Webster and Bair[4]
O2*V3	O		O2*V1	O		3.50E-12	0.0	0.	Webster and Bair[4]
O2*V3	O		O2*V2	O		3.50E-12	0.0	0.	Webster and Bair[4]
O2*V4	O		O2	O		8.00E-12	0.0	0.	Webster and Bair[4]
O2*V4	O		O2*V1	O		4.00E-12	0.0	0.	Webster and Bair[4]
O2*V4	O		O2*V2	O		4.00E-12	0.0	0.	Webster and Bair[4]
O2*V4	O		O2*V3	O		1.80E-12	0.0	0.	Webster and Bair[4]
O2(SG)	O2		O2*V1	O2*V1		8.00E-16	0.0	0.	Bortner[10]
O2(SG)	O2		O2*V3	O2		8.00E-16	0.0	0.	Bortner[10]
O2*V1	O3		O2	O3		4.40E-13	0.0	0.	Webster and Bair[4]
O2*V2	O3		O2	O3		5.00E-13	0.0	0.	Webster and Bair[4]
O2*V2	O3		O2*V1	O3		2.50E-13	0.0	0.	Webster and Bair[4]
O2*V3	O3		O2	O3		1.40E-12	0.0	0.	Webster and Bair[4]
O2*V3	O3		O2*V1	O3		7.00E-13	0.0	0.	Webster and Bair[4]
O2*V3	O3		O2*V2	O3		7.00E-13	0.0	0.	Webster and Bair[4]
O2*V4	O3		O2	O3		1.60E-12	0.0	0.	Webster and Bair[4]
O2*V4	O3		O2*V1	O3		8.00E-13	0.0	0.	Webster and Bair[4]
O2*V4	O3		O2*V2	O3		8.00E-13	0.0	0.	Webster and Bair[4]
O2*V4	O3		O2*V3	O3		3.60E-13	0.0	0.	Webster and Bair[4]
O2*V1	M		O2	M		8.80E-15	0.0	0.	Estimate
O2*V2	M		O2	M		1.00E-14	0.0	0.	Estimate
O2*V2	M		O2*V1	M		5.00E-15	0.0	0.	Estimate
O2*V3	M		O2	M		2.80E-14	0.0	0.	Estimate
O2*V3	M		O2*V1	M		1.40E-14	0.0	0.	Estimate
O2*V3	M		O2*V2	M		1.40E-14	0.0	0.	Estimate
O2*V4	M		O2	M		3.20E-14	0.0	0.	Estimate
O2*V4	M		O2*V1	M		1.60E-14	0.0	0.	Estimate
O2*V4	M		O2*V2	M		1.60E-14	0.0	0.	Estimate
O2*V4	M		O2*V3	M		7.20E-15	0.0	0.	Estimate
O3(AL)	M		O3	M		2.00E-15	0.0	0.	von Rosenberg and Trainor[24]
O	O2(SG)		O(1D)	O2		3.39E-11	-.1	4201.	Reverse
O2	M		O2(SG)	M		9.86E-16	.0	18549.	Reverse
O2(SG)	+ hv		O	O					Estimate
O2*V1	+ hv		O	O					Estimate
O2*V1	+ hv		O	O(1D)					Krupenie[7]
O2*V2	+ hv		O	O					Estimate
O2*V2	+ hv		O	O(1D)					Krupenie[7]
O2*V3	+ hv		O	O					Estimate
O2*V3	+ hv		O	O(1D)					Krupenie[7]
O2*V4	+ hv		O	O					Estimate
O2*V4	+ hv		O	O(1D)					Krupenie[7]
O3	+ hv		O	O2*V2					Ackerman[22]

Reactants		Products		A	B	C	References
O3	+ hv	O2*V3	O(1D)				Ackerman[22]
O2*V1	+ hv	O2*V2					Krupenie[7]
O2*V1	+ hv	O2*V3					Krupenie[7]
O2*V1	+ hv	O2*V4					Krupenie[7]
O2*V2	+ hv	O2*V1					Krupenie[7]
O2*V2	+ hv	O2*V3					Krupenie[7]
O2*V2	+ hv	O2*V4					Krupenie[7]
O2*V3	+ hv	O2*V1					Krupenie[7]
O2*V3	+ hv	O2*V2					Krupenie[7]
O2*V3	+ hv	O2*V4					Krupenie[7]
O2*V4	+ hv	O2*V1					Krupenie[7]
O2*V4	+ hv	O2*V2					Krupenie[7]
O2*V4	+ hv	O2*V3					Krupenie[7]
O2-	Air+	NO	O2*V4	2.80E-08	-.5	(3E-25)	Estimate
O2-	Air+	O2	O2*V4	3.90E-07	-.5	(3E-25)	Estimate

APPENDIX B

CHEMICAL EQUILIBRIA FOR T > 5000 K

For the temperature range 5000 to 20000 K, the chemical composition is computed with the assumption that the only species present are N_2, O_2, H_2O, N, O, H, NO, OH, NO_2, HO_2, O_3, e^-, N^+, NO^+, O^+, and H^+, and they are in thermodynamic equilibrium.

The equilibria among these 14 species are computed as needed in the course of the main computation. This is done with a subroutine that minimizes the total Gibbs free energy, subject to appropriate constraints, using Lagrange multipliers.

When the temperature exceeds 20 000 K, doubly charged ions begin to be important and molecules are no longer present. Under these circumstances, we can calculate an approximate composition from the equation-of-state tables, which were generated via detailed Saha equilibrium computations. From the pressure and temperature, we calculate the total particle density, $n = P/kT$. From the density and average atomic mass (14.45 amu), we get the number density of atoms and ions, $n_{nuclei} = \rho\sqrt{m}$. The number density of electrons is $n_e = n - n_{nuclei}$. We then assume $n_{AIR+} = n_e$, $n_N \sim 0.8(n_{nuclei} - n_{AIR+})$, and $n_O \sim 0.2(n_{nuclei} - n_{AIR+})$.

REFERENCES

1. B. F. Myers and M. R. Schoonover, "UV Photon and Electron Deposition in the Atmosphere," Science Application Inc., Defense Nuclear Agency Report DNA 4068F (30 June 1976).

2. H. E. DeWitt, "A Compilation of Spectroscopic Observations of Air Around Atomic Bomb Explosions," Los Alamos Scientific Laboratory report LA-1935-MS (June 1955).

3. V. D. Baiamonte, L. G. Hartshorn and E. J. Bair, "Ozone Ultraviolet Photolysis. III. Disposition of Vibrational Energy, " J. Chem. Phys, $\underline{55}$, 3617-3623 (1971).

4. H. Webster III and E. J. Bair, "Ozone Ultraviolet Photolysis. IV., $O_2{}^* + O(^3P)$ Vibrational Energy Transfer," J. Chem. Phys., $\underline{56}$, 6104-6108 (1972)

5. J. Zinn and C. D. Sutherland, "Special Numerics for a Nuclear Fireball Model, " Los Alamos National Laboratory report LA-9413-MS (June 1982).

6. J. Zinn, "A Finite Difference Scheme for Time-Dependent Spherical Radiation Hydrodynamics Problems," J. Comp. Phys., $\underline{13}$ 569-590 (1973).

7. P. H. Krupenie, "The Spectrum of Molecular Oxygen," J. Phys. Chem. Ref. Data, $\underline{1}$, 423-534 (1972).

8. C. K. Mitchell, E G & G - LAO (unpublished computations).

9. J. J. Griffin, "Beta Decays and Delayed Gammas from Fission Fragments" Los Alamos Scientific Laboratory report LA-2811 (December 62) Also LA-2811 Addendum I (October 1963) and Addendum II (April 1964).

10. M. H. Bortner and J. Baurer, eds., Defense Nuclear Agency Reaction Rate Handbook, Second Edition, Rev. No. 7, DNA 1948H (1978).

11 R. F. Hampson and D. Garvin, eds., National Bureau of Standards Special Publication 513 (1978).

12. L. G. Anderson, "Atmospheric Chemical Kinetics Data Survey," Am. Geophys. Union, $\underline{14}$, No. 2 (May 1976).

13. W. B. Demore, ed., "Chemical Kinetic and Photochemical Rate Data for Use in Stratospheric Modelling," NASA/Jet Propulsion Laboratory Publication 79-27 (1979).

14. W. J. Marinelli and H. S. Johnston, "Reaction Rates of Hydroxyl Radical with Nitric Acid and with Hydrogen Perioxide," to be published in J. Chem. Phys.

15. C. J. Hochanadel, T. J. Sworski, and P. U. Ogren, "Rate Constants for the Reactions of HO_2 with OH and with HO_2," J. Phys. Chem., $\underline{84}$, pp. 3274-3277 (1980).

16. P. J. Crutzen, "Ozone Production Rates in an Oxygen-Hydrogen-Nitrogen Oxide Atmosphere, J. Geophys. Res., $\underline{76}$, 7211 (1971).

17. H. S. Johnston and R. Graham, "Photochemistry of NO_X and HNO_X Compounds," Can J. Chem., $\underline{52}$, 1415 (1974).

18. D. Garvin, ed., "Chemical Kinetics Data Survey, V.," National Bureau of Standards report NBSIR 73-206 (1973).

19. W. F. Huebner and C. W. Carpenter, "Solar Photo Rate Coefficients," Los Alamos Scientific Laboratory report LA-8085-MS (October 1979).

20. W. C. Schumb, C. N. Gatterfield, and R. L. Wentworth, Hydrogen Peroxide, Reinhold, New York (1955).

21. J. H. Park, "The Equivalent Mean Absorption Cross Sections for O_2 Schumann-Runge Bands: Application to the H_2O and NO Photodissociation Rates," J. Atm. Sci., $\underline{31}$, p. 1893 (1974).

22. M. Ackerman, "Ultraviolet Solar Radiation Related to Mesospheric Processes," in Mesospheric Models and Related Experiments, G. Fiocco, ed., Proc. 4th ESRIN-ESLAB Symp., Frascati, Italy, July 1970 (Reidel, Dordrecht-Holland, 1970).

23. P. Warneck, "Laboratory Measurements of Photodetachment Cross Section of Selected Negative Ions (final report)," Geophys. Corp. Am. report GCA-TR-69-13-N (June 1969).

24. C. W. von Rosenberg, Jr. and D. W. Trainor, "Vibrational Excitation of Ozone Formed by Recombination," J. Chem. Phys., $\underline{61}$ (September 1974).

Page Range	NTIS Price Code	Page Range	NTIS Price Code	Page Range	NTIS Price Code	Page Range	NTIS Price Code
001-025	A02	151-175	A08	301-325	A14	451-475	A20
026-050	A03	176-200	A09	326-350	A15	476-500	A21
051-075	A04	201-225	A10	351-375	A16	501-525	A22
076-100	A05	226-250	A11	376-400	A17	526-550	A23
101-125	A06	251-275	A12	401-425	A18	551-575	A24
126-150	A07	276-300	A13	426-450	A19	576-600	A25
						601-up*	A99

*Contact NTIS for a price quote.

Los Alamos